Journal of Computational Physics 228 (2009) 6456–6478

Contents lists available at ScienceDirect

Journal of Computational Physics

journal homepage: www.elsevier.com/locate/jcp

An interaction potential based lattice Boltzmann method with adaptive mesh refinement (AMR) for two-phase flow simulation

Zhao Yu, Liang-Shih Fan *

Department of Chemical and Biomolecular Engineering, The Ohio State University, 140 West 19th Avenue, Columbus, OH 43210, USA

ARTICLE INFO

Article history:
Received 6 February 2009
Received in revised form 20 May 2009
Accepted 23 May 2009
Available online 30 May 2009

Keywords:
Lattice Boltzmann method
Adaptive mesh refinement
Multiphase flow
Bubble
Interaction potential

ABSTRACT

The lattice Boltzmann method (LBM) for two-phase flow simulation is often hindered by insufficient resolution at the interface. As a result, the LBM simulation of bubbles in bubbling flows is commonly limited to spherical or slightly deformed bubble shapes. In this study, the adaptive mesh refinement method for the LBM is developed to overcome such a problem. The approach for this new method is based on the improved interaction potential model, which is able to maintain grid-independent fluid properties in the two-fluid phases and at the interface. The LBM–AMR algorithm is described, especially concerning the LBM operation on a non-uniform mesh and the improved interaction potential model. Numerical simulations have been performed to validate the method in both single phase and multiphase flows. The 2D and 3D simulations of the buoyant rise of bubbles are conducted under various conditions. The agreement between the simulated bubble shape and velocity with experiments illustrates the capability of the LBM–AMR approach in predicting bubble dynamics even under the large bubble deformation conditions. Further, the LBM–AMR technique is capable of simulating a complex topology change of the interface. Integration of LBM with AMR can significantly improve the accuracy and reduce computation cost. The method developed in this study may appreciably enhance the capability of LBM in the simulation of complex multiphase flows under realistic conditions.

1. Introduction

The phenomena of two-phase flows with dynamic interfaces are ubiquitous in daily life. Such phenomena are also present in many industrial systems. Gas bubbles and liquid droplets are typical forms of such two-phase flows. Understanding the dynamics of these deformable fluid particles is crucial to the design and operation of many two-phase flow devices ranging from microfluidic devices to large systems such as bubble columns and three-phase fluidized beds [1]. Due to its importance in applications to multiphase reactor systems, the dynamics of droplets and bubbles has been studied extensively using experimental methods and mathematical models [2,3]. Many experimental studies were, however, limited by the difficulties in monitoring the moving interface and the detailed flow field in precise controlled experimental conditions. The computational studies were also challenged by the numerical stability problems in the flow field near the moving interface in some bubbling flow regimes. Recent advances in direct numerical simulation (DNS) provide a promising approach to the simulation of bubble and droplet dynamics in a more accurate manner. In DNS, the motion and deformation of each individual droplet or bubble are directly resolved, together with the flow in both phases, providing a complete and detailed picture of the flow field. The DNS results not only allow parametric studies of different effects on the droplet/bubble behavior under well-controlled conditions, but can also provide the missing closure information for the two-phase interactions in the

* Corresponding author.
E-mail address: fan.1@osu.edu (L.-S. Fan).

0021-9991/$ - see front matter © 2009 Elsevier Inc. All rights reserved.
doi:10.1016/j.jcp.2009.05.034

averaged two-fluid model, which will ultimately be applied to simulate the entire reactor that involves a large number of fluid particles.

Several types of DNS methods have been already developed and applied to the simulation of two-phase flow problems. In general, all of these DNS methods have three basic ingredients: the interface algorithm, the flow solver, and the mesh. The interface algorithm provides a way to represent the interface that separates different fluid phases with different properties. The flow solver solves for the flow field in all phases, and the velocity field is coupled with the interface algorithm to update the location of the interface. All the numerical operations are performed on a mesh that discretizes the computation domain. In each of the above three categories, there are several techniques of choice, and many existing DNS methods can be regarded as different combinations of these ingredients.

There are two basic approaches to treat the interface between two-fluid phases: the diffused interface model [4], and the sharp interface model. In the diffused interface model, the interface has a finite width, and fluid properties are allowed to vary smoothly across the interface according to thermodynamic principles. A typical technique involving this approach is the phase-field model [5]. On the other hand, in the sharp interface model, the two-fluid phase domains are jointed conceptually by an infinitesimally thin boundary with jump conditions across the interface, and this approach can be further divided into the front-tracking method and the front-capturing method. In the front-tracking method [6], the interface is explicitly represented by a surface mesh, which is made up of Lagrangian particles that are convected by the local flow field in each time step to update the location of the interface. In the front-capturing approaches the interface is represented implicitly by the contour of a scalar function. The most popular front-capturing techniques include the volume of fluid (VOF) method [7], and the level-set method (LSM) [8]. The scalar field in these cases is either the volume fraction of the gas phase in the computational cell (in VOF), or the distance to the interface (in LSM). In actual computation, however, the interfaces in both the physically sharp interface model and the diffused interface model are numerically smeared out [9]. The difference between them is that, for the sharp interface method the properties are merely numerically interpolated across the interface, while the distributions of the properties in the diffused interface method are determined by the thermodynamic law. At the same time, the interface width in the sharp interface is usually smaller than that in the diffused interface model.

The flow field can be solved using either the Navier–Stokes (N–S) equation or the lattice Boltzmann equation. Different from most fluid simulation methods that are rooted in the N–S equation, which is the momentum conservation on the continuum level, the lattice Boltzmann method (LBM) focuses on the discrete particles that comprise the fluid, and calculates the evolution of the particle distribution function. While it is formally related to the classic Boltzmann equation in non-equilibrium statistical mechanics, it can also be proved that the LB equation recovers the N–S equation for the macroscopic flow in the incompressible limit. This makes LBM a mesoscopic method and therefore can simulate problems with more complicated physics than the N–S based methods. The extension of kinetic theory-based LBM beyond N–S equation has also been recently reported for complex flows with high Mach number, high Knudsen number, and non-Newtonian fluids [10]. In addition, the algorithm in LBM is much simpler than that in traditional CFD methods, and parallel computation can be implemented with ease [11]. For the simulation of multiphase flows with dynamic interfaces, three main types of LBM techniques have been already developed. Among them, both the interaction potential model [12] and the free-energy model [13] employ the idea of diffused interface methods, while the color function model [14] is closer to the concept of sharp interface methods. By introducing inter-particle forces to the original "collision–propagation" dynamics of ideal gas particles in LBM, the interaction potential model is able to describe the behavior of dense fluids. The interaction potential relates the microscopic interaction forces to a non-ideal gas equation of state, which determines the phase separation properties according to thermodynamics. In this way, the interaction potential model has a clear physical background that is consistent with the kinetic theory and original LBM, and maintains the simplicity in algorithm. In addition, the interface is formed spontaneously due to the phase separation resulted from particle interactions, and consequently no interface tracking or capturing is necessary. Therefore, the interaction potential model is chosen as the two-phase LBM of interest in this study.

Regardless of the numerical approach used, the central problem in the direct simulation of two-phase flows is the accurate representation of the gas–liquid interface. As already mentioned, all numerical approaches use a numerically diffused interface, which spans typically to a thickness of 3–5 grid spacing. On the other hand, taking a bubble rising in liquid as an example, the simulated bubble size must be significantly larger than the interface thickness in order to have sufficient accuracy. For bubbles with small deformation, at least 16 grid points across the diameter are usually required to faithfully represent the bubble. This minimum grid number increases when the bubble undergoes larger deformation, for example, in higher Reynolds number flows. At the same time, the simulation domain needs to be significantly larger than the bubble size to avoid boundary effects, and the computation time and memory usage increase rapidly with the increasing mesh resolution and domain size. However, under current computation capability, this resolution requirement often has to be compromised. As the result, most simulations to date consider only small bubbles with spherical or ellipsoidal shapes, while simulations for large spherical cap and skirted bubbles that frequently appear in engineering applications are scarcely reported. Moreover, in numerical studies which explore the bubble interactions, the number of bubbles that can be put into the simulation domain is also restricted due to the computation power. Consequently, there is a demand for a simulation technique that can simultaneously achieve sufficient mesh resolution near the bubble surface, while maintaining the total computation cost under control.

Adaptive mesh refinement (AMR) technique is a natural candidate to meet such requirement in both resolution and computation cost. Using AMR technique, the mesh resolution varies in the computation domain. Fine mesh resolution is used

near the bubble surface to ensure the accuracy, while coarse mesh is applied in the bulk fluid faraway from the interface to reduce computation cost. The mesh resolution is updated dynamically during the simulation in accordance with the motion of the interfaces. There have been a few studies that integrate AMR into incompressible fluid-phase flow models based on N–S equation. Ginzburg and Wittum [15] performed 2D simulation of bubbles using VOF approach with AMR. The mesh near the interface is further split, and unstructured mesh that is aligned with the interface is used to solve the VOF equation, while the flow equations are solved on a separate regular mesh. The level-set technique has been coupled with AMR by Sussman et al. [16] and Olsson et al. [17]. Two- and three-dimensional simulations were performed in example problems involving droplets and bubbles. Recently, Hua et al. [18] combined the front-tracking method with AMR and successfully simulated a wide range of bubble regimes which compare well with well-known experimental results. In particular, large deformation of the bubble surface in spherical cap regime and skirted regime can be accurately reproduced.

Although the original LBM algorithm is closely coupled with a uniform mesh, recently some research has been conducted to extend the method to non-uniform grids, mainly for the modeling of single phase flows. In these works, the computation domain consists of multiple blocks with variable grid sizes; although within each block the mesh remains uniform and structured. Communication between blocks with different grid size depends on the exact location of the particle distributions. If the distributions reside on the grid nodes, usually a special interpolation procedure will be necessary to rescale the non-equilibrium part of the distribution [19–22]. If a volumetric formulation is used and the distributions are located at cell center, however, no such rescaling is required [23–25]. In the above simulations, fine mesh is applied near the irregular solid boundary to enhance the accuracy of the boundary condition, or near the high-vorticity region to resolve the complex flow field. Since they do not involve moving objects, the mesh resolution is specified in the beginning of the simulation, without being dynamically updated. Despite the promising results obtained for single phase flows, there is no straightforward extension of the non-uniform grid LBM algorithm to two-phase flow problems. There seems to be only one publication concerning the multiphase LBM–AMR [26]. In that study, the interface algorithm was based on the color function model, and therefore was similar to the interface capturing methods. Only a single condition of bubble rising was demonstrated in the result, without experiment comparison for broader regimes.

In this study, a new LBM–AMR approach is developed for the gas–liquid flows. The two-phase LBM is based on the interaction potential model developed by Shan and Chen [12]. Due to its diffuse-interface nature, the properties across the interface are determined by the thermodynamics. Therefore, it is essential to have consistent fluid properties on different sized grids, which is different from the LBM–AMR with sharp interface model developed by Tolke et al. [26]. The LBM algorithm on a uniform mesh will be briefly discussed in the next section, followed by its extension to non-uniform gird for single phase flows, which is presented in Section 3. The relationship between interface properties in the interaction potential model and the grid size is discussed in Section 4. Section 5 presents a series of numerical results for the buoyant rise of bubbles in a viscous liquid. A broad range of conditions are reported including both 2D and 3D cases, and a good agreement between the numerical and experimental results proves the validity of the newly developed method.

It is noted that the conventional two-phase LBM also suffers from other limitations, mainly the numerical instability at high density ratios and low viscosities. Fortunately, various methods have been proposed in recent years to enhance its stability under those conditions. For example, the stability at high density ratio can be improved by using more realistic equations of state [27], employing pressure Poisson equation [28], or using pressure evolution formulation of the LBM [29]. The stability at low viscosity can be achieved with implicit LBM formulation [30] or multi-relaxation-time (MRT) approach [31]. Combination of these advanced techniques with the AMR has the potential to greatly expand the accessible parameter range of the two-phase LBM, and therefore enhance its capability for simulating a wide range of multiphase flow problems which are directly relevant to real-world engineering practice.

2. LBM algorithm on a uniform grid

The LBM algorithm is based on a special discretization of the Boltzmann equation in time, space, and velocity space. The main variable in LBM algorithm is $f_i(\mathbf{x}, t)$, which is the density distribution of the pseudo fluid molecules that has lattice velocity $\mathbf{c}_i$ at location $\mathbf{x}$ and time t. The evolution of the distribution function obeys the lattice Boltzmann equation:

$$f_i(\mathbf{x}+\mathbf{c}_i\Delta t, t+\Delta t) - f_i(\mathbf{x}, t) = -\frac{1}{\tau}\left[f_i(\mathbf{x}, t) - f_i^{(eq)}(\rho, \mathbf{u})\right] \tag{1}$$

The left-hand side of Eq. (1) is often called "streaming" or "propagation", and accounts for the migration of the fluid molecule from one grid point to its neighboring point. The right-hand side is often named "collision", and models the relaxation process of the molecules towards to the local equilibrium distribution $f_i^{(eq)}$, which is the truncated Boltzmann distribution:

$$f_i^{(eq)}(\rho, \mathbf{u}) = \rho w_i\left[1 + \frac{\mathbf{c}_i\cdot\mathbf{u}}{c_s^2} + \frac{(\mathbf{c}_i\cdot\mathbf{u})^2}{2c_s^4} - \frac{\mathbf{u}^2}{2c_s^4}\right] \tag{2}$$

The macroscopic variables such as fluid density and momentum are related to the distribution function is such a way that

$$\rho(\mathbf{x}, t) = \sum_i f_i(\mathbf{x}, t), \quad \rho\mathbf{u}(\mathbf{x}, t) = \sum_i \mathbf{c}_i f_i(\mathbf{x}, t) \tag{3}$$

The pressure and kinematic viscosity are given as:

$$p = \rho c_s^2 \tag{4}$$

$$\nu = \left(\tau - \frac{1}{2}\right)\Delta t c_s^2 \tag{5}$$

where τ is the non-dimensional relaxation factor in Eq. (1), and $c_s = \frac{1}{\sqrt{3}}\frac{\Delta x}{\Delta t}$ is the lattice sound speed.

In practice, the variables in LBM are non-dimensionalized using Δx and Δt as the length and time scales. As the result, the non-dimensional mesh size and time step are both equal to 1.

3. Single phase LBM with non-uniform mesh

When applying different mesh resolutions inside the computation domain, it is crucial to determine which variables change with the mesh size and which variables are independent of the grid. In order to achieve the same lattice speed of sound $c_s = \frac{1}{\sqrt{3}}\frac{\Delta x}{\Delta t}$ across the entire domain, the time step needs to be proportional to the mesh size. Following the convention of LBM, the non-dimensional lattice speed of sound is kept to be $\hat{c}_s = \frac{1}{\sqrt{3}}$ throughout the entire domain.

The fact that the time step Δt varies with Δx has two consequences. Firstly, according to Eq. (5), to keep the fluid kinematic viscosity ν independent of grid size, the relaxation factor τ also has to be adjusted with Δx and must be calculated from Eq. (5). Explicitly, this requires

$$\tau_f - \frac{1}{2} = \left(\tau_c - \frac{1}{2}\right)\frac{\Delta x_c}{\Delta x_f} \tag{6}$$

Secondly, the LBM algorithm performs more steps on the fine mesh since it requires a smaller Δt than on the coarse mesh. Therefore, interpolation/average operations need to be performed at the coarse/fine resolution interface in both space and time.

The newly developed LBM–AMR approach is based on the multi-block structured grid. The entire computation domain is divided into a number of blocks that have identical grid structure but may have different grid sizes. The blocks are categorized into different refinement levels, and grid resolutions in each two consecutive levels differ by a factor of 2. In order to have a smooth transition of the grid size, at most one refinement level difference is allowed at the boundary between two neighboring blocks. Inside each block, uniform structured grid is used as in the traditional LBM simulation. In this way, the original LBM algorithm can be applied within each individual block without modification. The classical D2Q9 lattice is employed for the 2D computations in this study, and the D3Q19 lattice is used for the 3D simulations.

When a refinement level jump is present between two neighboring blocks, a special algorithm is devised to communicate the information across block boundaries. Similar to the volumetric formulation of Rohde et al. [23], the particle distributions in the current method are located at the center of each computational cell, so that rescaling of the non-equilibrium part of the distribution at coarse/fine grid interface is not necessary. The inter-block communication process is shown schematically

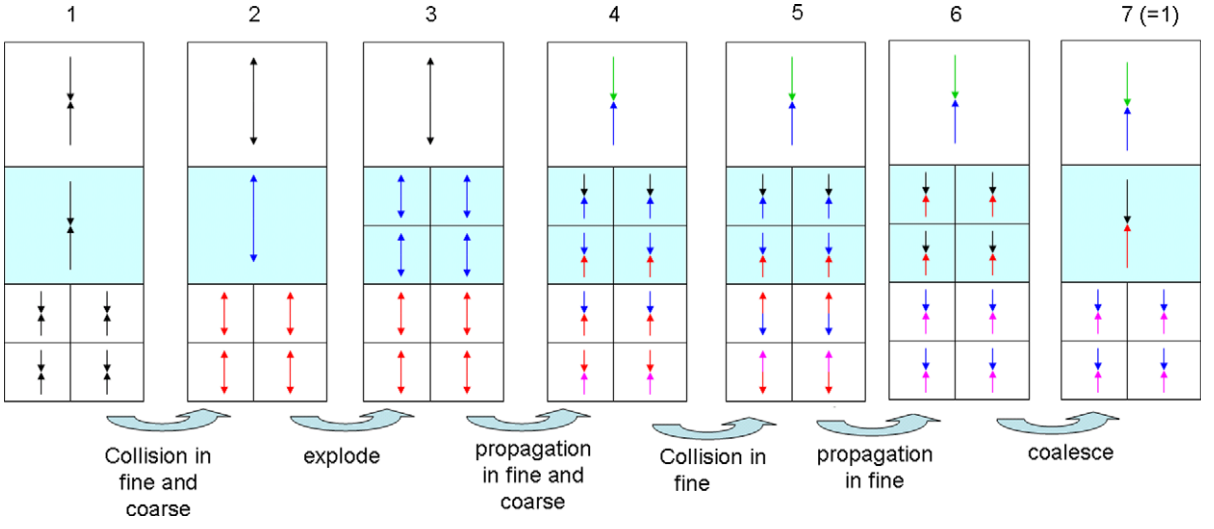

Fig. 1. Schematic illustration of the change of particle distributions in the cells near the refinement jump in a 2D computation. For simplicity, only a single pair of particle distributions is shown. The arrows pointing towards the cell center represent the "pre-collision" distributions, while the arrows pointing away from the cell center represent the "post-collision" distributions.

in Fig. 1. The computational cells at the boundary between the coarse and fine grid are referred to as the "interface" cells, as shown in the shaded zones in Fig. 1.They act as the transition layer between two blocks, and alternate between coarse and fine levels during a computation step through splitting and merging. Two specially designed operations take place in these interface cells, and they are named "explosion" and "coalescence" after the terminology used by Chen et al. [24]. In the 2D example illustrated in Fig. 1, a coarse interface cell is uniformly divided into four smaller cells during the explosion step (steps 2–3 in Fig. 1), and its particle population is either evenly distributed or linearly interpolated in these new cells. In the coalescence step (steps 6–7 in Fig. 1), the four fine interface cells again merge into a single coarse level cell, whose particle population is the summation of those in the four fine cells.

The original "collision–propagation" algorithm is now complicated by the additional "explosion" and "coalescence" operations. The flowchart of the computation procedure on a mesh with two refinement levels is shown in Fig. 2. As noted previously, the computation on coarse level uses dt as its time step, while the fine grid has the time step of $0.5dt$. Therefore, the "collision–propagation" operations happen twice on the fine level in each dt, but only once on the coarse level. The "explosion" and "coalescence" steps each operates once during dt. The "explosion" takes place after the first collision step at $0.5dt$, which transfers the information from coarse level to the fine level. And the "coalescence" happens at the end of the time step so as to pass the information back from the fine level to the coarse level.

The change of particle distributions in each sub-step is illustrated graphically in Fig. 1, in which only one pair of opposing lattice velocities are shown for clarity. The first collision step operates on both fine and coarse levels as in ordinary LBM, but with different relaxation parameters. The interface cells, which are originally on the coarse level, are then divided into 4 fine cells in the "explosion". The distribution functions f_i can be either uniformly distributed or interpolated linearly in the new fine cells. Propagation step then occurs on both coarse and fine level, including the interface cells. Up to this point, the coarse level has completed a time step dt, while the fine level only completes a half dt. Therefore, the second collision and propagation process only occurs on the fine level, and distribution functions only change on the fine and interface cells while the information on the coarse level is unaffected. Finally, the four fine interface cells again merged into a coarse level cell, and the distribution functions in the new coarse interface cell is just the sum of those in the four fine cells. This finishes the entire computation loop and both levels come back to the pre-collision status before step 1.

The generation and refinement of the mesh is performed with the open-source code PARAMESH [32], which uses a tree data structure to manage the hierarchy of block-structured grid with different refinement levels. It has been integrated with the non-uniform grid LBM code developed by the authors.

The above LBM algorithm for non-uniform mesh is validated by simulating two simple flow conditions: the Couette flow driven by shear force and the Poiseuille flow driven by pressure gradient. Both cases use two levels of grid refinement, as shown in Fig. 3(a) and (c). For the simple shear flow, the fine grids are applied in the lower half of the domain near the stationary wall, and in the pressure driven flow the fine grids are applied near both top and bottom walls. Periodic conditions are used in the horizontal direction, and bounce-back conditions are used at the wall boundaries. The velocity profiles are shown in Fig. 3(b) and (d). The simulated profiles are in good agreement with the analytical results. Especially, both the velocity and the stress are continuous at the interface between coarse and fine grids. In addition to the conditions where the coarse/fine grid interface is parallel to the flow direction, Fig. 3(e) and (f) present the Poiseuille flow simulation with grid interface perpendicular to the flow direction. In this simulation, 80×80 grid is used in the region $0 < x < 40$, while 40×40 resolution is applied in the region $40 < x < 80$. Velocity profiles across the channel extracted at $x = 10$ for the fine resolution region and $x = 60$ for the coarse grid region are compared against the analytical curve. The two numerically obtained profiles are both in good agreement with the analytical profile. While the coarse grid give the maximum velocity $u_m = 0.001965$ at $y = 20$, the fine grid results in $u_m = 0.00199$. Since the theoretical maximum velocity is 0.002, numerical errors with both the coarse and fine grids are within 2%. The result obtained with the fine grid is closer to the theoretical value, due to the fact that the current LBM algorithm with link bounce-back boundary condition has second order spatial accuracy.

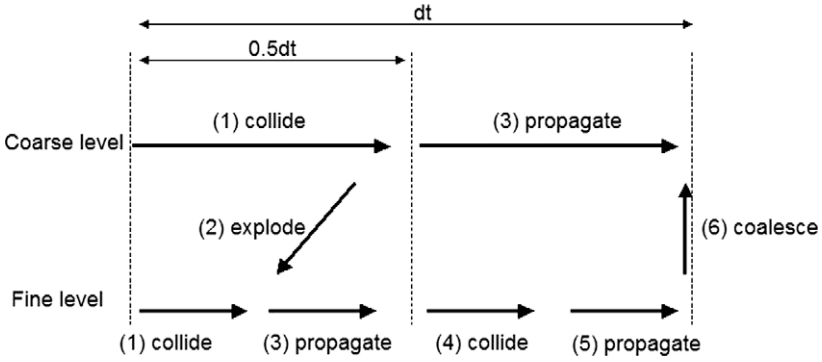

Fig. 2. Flowchart of the computation procedure during one time step for two refinement levels. The sequence of sub-steps (1–6) is in accordance with those in Fig. 1.

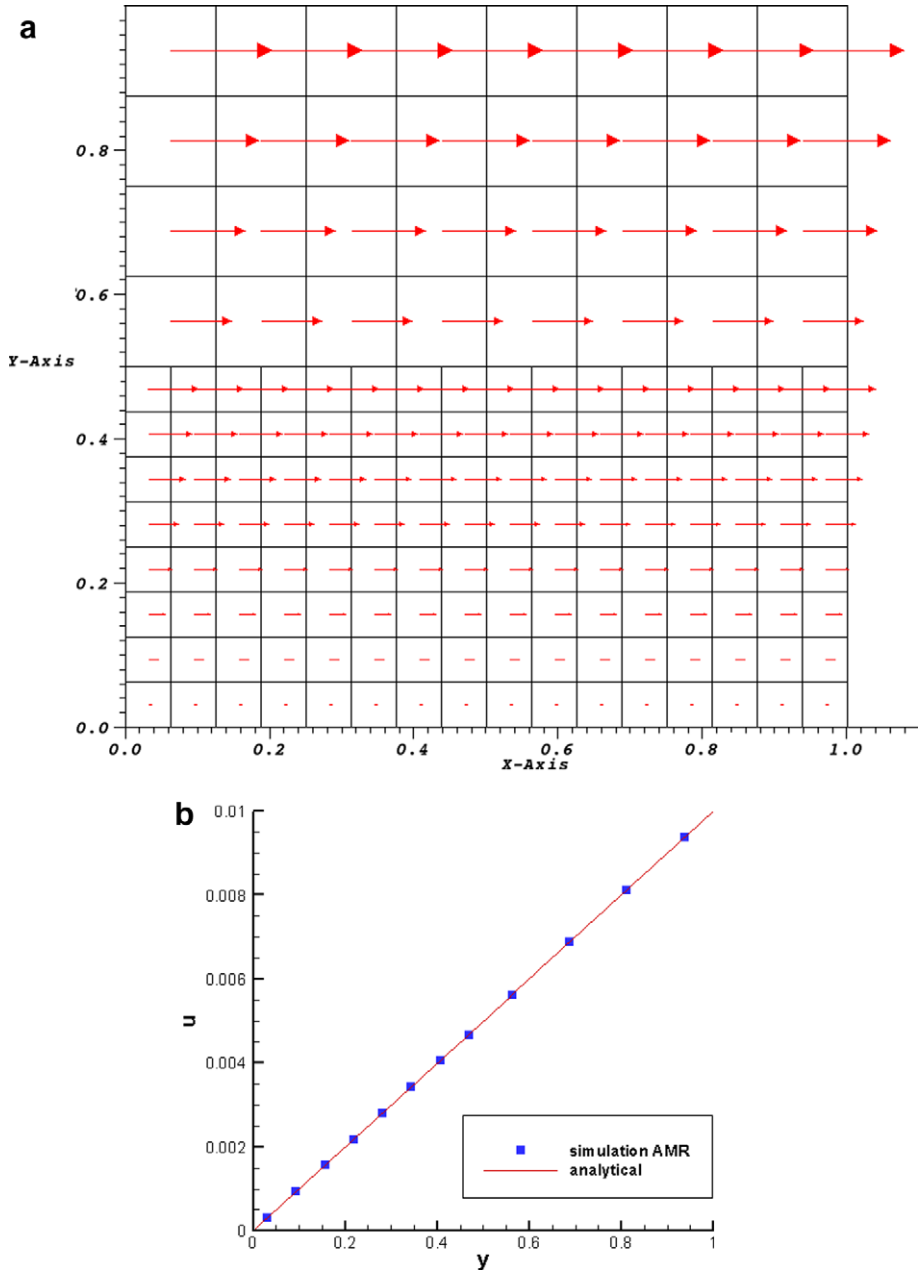

Fig. 3. Results of single phase flow obtained using LBM–AMR. (a) Grid arrangement and velocity field for Couette flow. (b) Comparison of simulated and analytical velocity profiles in Couette flow. (c) Grid for Poiseuille flow with grid interface parallel to the flow direction. (d) Velocity profiles in Poiseuille flow with grid interface parallel to the flow direction. (e) Grid for Poiseuille flow with grid interface perpendicular to the flow direction. (f) Velocity profiles in Poiseuille flow with grid interface perpendicular to the flow direction.

4. Two-phase LBM based on interaction potential model

4.1. Equilibrium and surface properties in interaction potential model

The interaction potential model developed by Shan and Chen [12] is employed for the two-phase flow simulation in this study. In this model the interaction forces between fluid molecules are accounted for base upon the inter-molecular interactions. In a single component fluid, the interaction forces convert the original ideal gas equation of state (EOS) in LBM into a non-ideal EOS, and therefore phase separation takes place spontaneously when the temperature falls below the critical temperature of the fluid. In a binary fluid mixture, both intra-species and inter-species interactions are incorporated into the model, which result in different distributions of the two components in two immiscible phases. For simplicity, only the

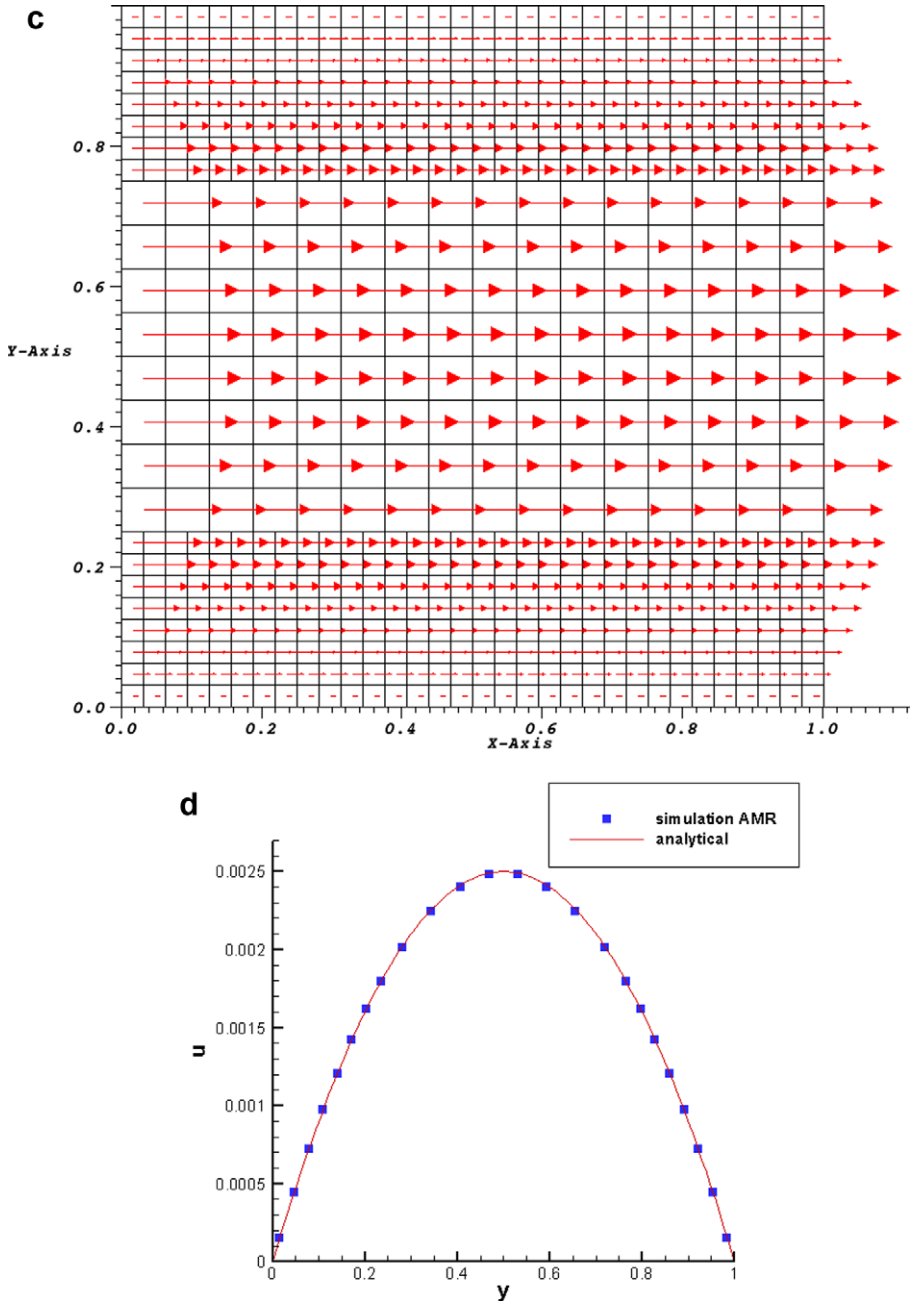

Fig. 3 *(continued)*

single component interaction model will be discussed in this section in order to illustrate how the interaction model can be integrated with the AMR algorithm.

The Shan–Chen model defines an interaction potential as a function of the local density of the fluid.

$$\psi = \psi(\rho(x)) \tag{7}$$

The interaction force on the fluid at grid location x is the sum of its pair-wise interactions with the nearest neighbors in each lattice direction:

$$\mathbf{F} = -G\psi \sum_i T_i \psi(\mathbf{x} + \mathbf{c}_i)\mathbf{c}_i/\Delta x \tag{8}$$

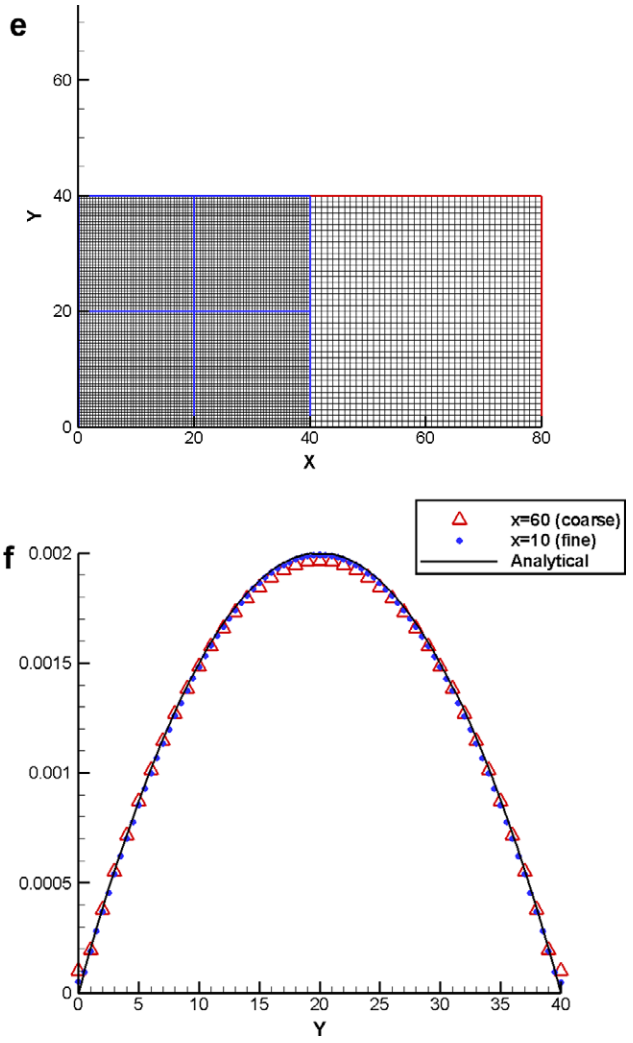

Fig. 3 *(continued)*

Here G is a constant representing the strength of the interaction, and T_i is the weight associated with different lattice directions. On the other hand, from a finite difference point of view, the above equation can also be interpreted as a finite difference stencil, and the following equation can be obtained by expanding Eq. (8) to the 2nd order:

$$\mathbf{F} = -\nabla\left(\frac{1}{2}c_s^2 G\psi^2\right) - \frac{1}{2}\Delta x^2 c_s^2 G\psi\nabla\nabla^2\psi + o(\Delta x^3) \tag{9}$$

It can be shown that the first term can be absorbed into the pressure term in the momentum equation and it results in a non-ideal EOS with the following expression:

$$p = \rho c_s^2 + \frac{1}{2}c_s^2 G\psi^2(\rho) \tag{10}$$

The second term in Eq. (9) represents the interface stresses corresponding to the gradient free energy, which has been used in both LBM and other types of diffuse interface models [5,33]. It is responsible for the structure of the interface as well as the surface tension. It should be noted that this force has a dependency of Δx^2, and is therefore dependent on the mesh resolution.

In thermodynamic theory, the EOS determines the bulk property of the fluid phase, and the equilibrium densities at a particular temperature can be located using techniques such as Maxwell construction [34]. The interface structure can be found by applying the mechanical equilibrium condition on the stress tensor across the interface, and the surface tension can be calculated from the stress profile

$$\sigma = \int_{-\infty}^{+\infty} (P_{zz} - P_{xx}) dz \tag{11}$$

In the above equation, the interface is assumed to lie in the x–y plane, and P_{zz} and P_{xx} are the stresses normal and parallel to the interface, respectively.

Due to the discrete lattice effects, the pressure tensor in LBM is slightly different from its counterpart in the macroscopic thermodynamics. The analytical solution of the interface structure and the value of surface tension in the interaction potential model have been reported recently by Shan [35]:

$$\left(\frac{d\rho}{dz}\right)^2 = \frac{8(1-\varepsilon)\psi^{\varepsilon}}{3Gc_s^4(\psi')^2\Delta x^2} \int_{\rho_g}^{\rho_l} \left(p(\rho) - \rho c_s^2 - \frac{1}{2}Gc_s^2\psi^2\right) \frac{\psi'}{\psi^{1+\varepsilon}} d\rho \tag{12}$$

$$\sigma = -\frac{3Gc_s^4 e_4 \Delta x^2}{2} \int_{-\infty}^{+\infty} \left(\frac{d\psi}{dz}\right)^2 dz \tag{13}$$

where ε and e_4 are constants depending on the lattice. With further analysis, it can be shown that in the original interaction potential model, both the interface width and the surface tension are proportional to the grid spacing Δx. Therefore, in order to have a consistent surface tension value, an additional term is necessary to compensate for the grid effect. In this study, the following additional term is introduced with a variable coefficient k, which is a function of grid size Δx.

$$\mathbf{F}^s = k\psi\nabla\nabla^2\psi \tag{14}$$

The above equation can be implemented using the pair-wise interaction between lattice sites in a similar way to the original Shan–Chen model:

$$\mathbf{F}^s(\mathbf{x}) = k\psi(\mathbf{x}) \sum_{\mathbf{y}} \lambda_{xy}\psi(\mathbf{y})\mathbf{r}_{xy}/\Delta x^3 \tag{15}$$

where $\mathbf{r}_{xy}$ is the vector pointing from $\mathbf{x}$ to $\mathbf{y}$, and λ_{xy} is the coefficient depending on $\mathbf{r}_{xy}$.

However, since the numerical evaluation of Eq. (14) requires a higher order difference operator for the interaction potential ψ, the summation in (15) needs to involve a larger set of lattice sites in addition to the nearest neighbors. There is a certain degree of freedom in choosing the set of the lattice sites and coefficients, and one example used in the 2D simulations in this study takes the form

$$\begin{aligned}\mathbf{F}^s_{x,ij} = \frac{k\psi_{i,j}}{\Delta x^3}\Big[&-\frac{5}{6}(\psi_{i+1,j} - \psi_{i-1,j}) + \frac{1}{6}(\psi_{i+2,j} - \psi_{i-2,j}) - \frac{1}{9}(\psi_{i+1,j+1} + \psi_{i+1,j-1} - \psi_{i-1,j+1} - \psi_{i-1,j-1}) \\ &+ \frac{5}{36}(\psi_{i+2,j+1} + \psi_{i+2,j-1} - \psi_{i-2,j+1} - \psi_{i-2,j-1}) + \frac{1}{36}(\psi_{i+1,j+2} + \psi_{i+1,j-2} - \psi_{i-1,j+2} - \psi_{i-1,j-2}) \\ &+ \frac{1}{36}(\psi_{i+2,j+2} + \psi_{i+2,j-2} - \psi_{i-2,j+2} - \psi_{i-2,j-2})\Big]\end{aligned} \tag{16}$$

$$\begin{aligned}\mathbf{F}^s_{y,ij} = \frac{k\psi_{i,j}}{\Delta x^3}\Big[&-\frac{5}{6}(\psi_{i,j+1} - \psi_{1,j-1}) + \frac{1}{6}(\psi_{i,j+2} - \psi_{i,j-2}) - \frac{1}{9}(\psi_{i+1,j+1} - \psi_{i+1,j-1} + \psi_{i-1,j+1} - \psi_{i-1,j-1}) \\ &+ \frac{1}{36}(\psi_{i+2,j+1} - \psi_{i+2,j-1} + \psi_{i-2,j+1} - \psi_{i-2,j-1}) + \frac{5}{36}(\psi_{i+1,j+2} - \psi_{i+1,j-2} + \psi_{i-1,j+2} - \psi_{i-1,j-2}) \\ &+ \frac{1}{36}(\psi_{i+2,j+2} - \psi_{i+2,j-2} + \psi_{i-2,j+2} - \psi_{i-2,j-2})\Big]\end{aligned} \tag{17}$$

It can be seen from (15) that the force exerted on fluid particles at location $\mathbf{x}$ due to their interaction with the fluid particles at $\mathbf{y}$ can be written as $k\lambda_{xy}\psi(\mathbf{x})\psi(\mathbf{y})\mathbf{r}_{xy}/\Delta x^3$, which has the same magnitude but opposite direction with the force on location $\mathbf{y}$ exerted by the particles at $\mathbf{x}$. Therefore, the total momentum of the entire domain is exactly conserved, which has been confirmed by the numerical simulations in this study.

As a result, the total interaction force is now

$$\mathbf{F} = \mathbf{F}^0 + \mathbf{F}^s \approx -\nabla\left(\frac{1}{2}c_s^2 G\psi^2\right) + \left(k - \frac{1}{2}\Delta x^2 c_s^2 G\right)\psi\nabla\nabla^2\psi \tag{18}$$

By using different value of k on different sized grids, the sum $k_0 = k - \frac{1}{2}\Delta x^2 c_s^2 G$ can be kept constant, and therefore a constant surface tension force can be achieved. In addition, compared to the original Shan–Chen model with only one parameter G, another parameter k is introduced, and therefore the surface tension can be tuned independent of the EOS, while bulk fluid properties at equilibrium are determined by G only. This is in fact similar to the concept of tuning the surface tension with two-parameter multi-range pseudo-potential [36].

Eq. (12) can be used to obtain the theoretical density profile across a flat interface at equilibrium. With the condition that the density gradient vanishes in both bulk phases, and that the equilibrium pressure is identical in both phases, Eq. (12) can be integrated numerically to find $\rho(z)$. Once the density profile is obtained, it can be used in Eq. (13) to find the theoretical value of the surface tension.

4.2. Forcing scheme

There are various ways to incorporate the interaction force into the LBM model. In the original Shan–Chen model, the force is incorporated by shifting the equilibrium velocity in the collision step.

$$\mathbf{u}^{\mathrm{eq}} = \mathbf{v} + \frac{\tau \Delta t \mathbf{F}}{\rho} \tag{19}$$

The macroscopic fluid velocity is given by averaging the momentum before and after the collision:

$$\mathbf{u} = \mathbf{v} + \frac{\Delta t \mathbf{F}}{2\rho} \tag{20}$$

In practice, it is found that with this forcing scheme the equilibrium pressure and densities vary when the relaxation parameter τ changes. As shown in the previous section, for a constant fluid kinematic viscosity, the value of the relaxation parameter τ is dependent on the grid resolution. Thus, the equilibrium properties of the same fluid will be different in sub-domains with different mesh sizes if the original Shan–Chen forcing scheme is used. This not only causes conceptual problems about inconsistent fluid property, but also leads to numerical instabilities due to the property mismatch at fine–coarse grid interface. Fortunately, by using some other forcing schemes, constant equilibrium properties can be maintained regardless of the value of τ. In this study, the forcing method of Guo et al. [37] is used, which has the form

$$f_i(\mathbf{x} + \Delta t \mathbf{c}_i, t + \Delta t) - f_i(\mathbf{x}, t) = -\frac{1}{\tau}[f_i(\mathbf{x}, t) - f_i^{(eq)}(\rho, \mathbf{u}^{\mathrm{eq}})] + K_i \tag{21}$$

The last term K_i is given by

$$K_i = \left(1 - \frac{1}{2\tau}\right) w_i \left[\frac{\mathbf{c}_i - \mathbf{u}^{\mathrm{eq}}}{c_s^2} + \frac{\mathbf{c}_i \cdot \mathbf{u}^{\mathrm{eq}}}{c_s^4}\mathbf{c}_i\right] \cdot \Delta t \mathbf{F} \tag{22}$$

And both the macroscopic fluid velocity and the equilibrium velocity are expressed in the same form:

$$\mathbf{u} = \mathbf{u}^{\mathrm{eq}} = \mathbf{v} + \frac{\Delta t \mathbf{F}}{2\rho} \tag{23}$$

4.3. Numerical results

A few numerical tests have been performed in order to demonstrate the above properties of the original Shan–Chen model and our improved interaction potential model. The original Shan–Chen model is made up of Eqs. (1), (2), (3), (8), (19) and

Table 1
Comparison of equilibrium densities and pressure obtained by forcing schemes developed by Guo et al. [37] and by Shan and Chen [12]. Simulation is conducted under constant interaction strength $G = -10$ and constant viscosity $\nu = 0.00025$, while τ changes as a function of dx. The analytical results from Eq. (12) are: $\rho_v = 0.3675, \rho_l = 2.7828, p = 0.1153$.

Δx	τ	Guo's forcing scheme			Shan–Chen forcing scheme		
		ρ_v	ρ_l	p	ρ_v	ρ_l	p
1/64	0.548	0.3677	2.783	0.1153	0.3681	2.784	0.1154
1/128	0.596	0.3667	2.781	0.1151	0.3680	2.784	0.1154
1/256	0.692	0.3673	2.782	0.1152	0.3737	2.794	0.1167
1/512	0.884	0.3663	2.782	0.1150	0.3890	2.819	0.1199
1/1024	1.268	0.3667	2.781	0.1151	0.4435	2.893	0.1295

Table 2
Equilibrium properties for different interaction strength G.

G	LBM simulation			Theoretical		
	Gas density	Liquid density	Pressure	Gas density	Liquid density	Pressure
−8.5	0.5198	1.9651	0.1430	0.5198	1.9651	0.1430
−9	0.4557	2.2494	0.1333	0.4558	2.2496	0.1333
−10	0.3670	2.7802	0.1151	0.3675	2.7828	0.1153
−11	0.3048	3.2938	0.0990	0.3053	3.2949	0.0992
−12	0.2601	3.7930	0.0858	0.2568	3.7980	0.0848

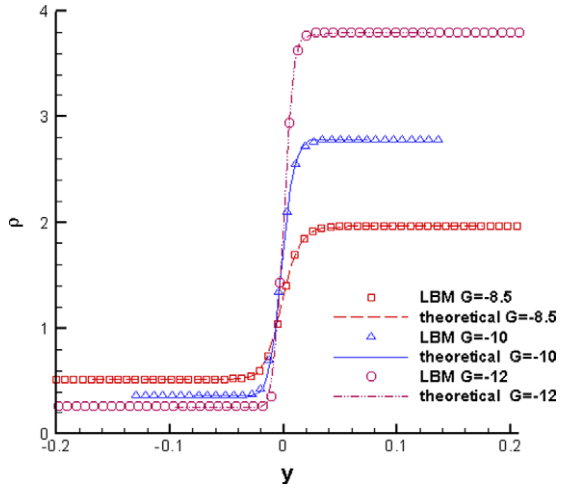

Fig. 4. Comparison of simulated and theoretical density profiles under different interaction strength.

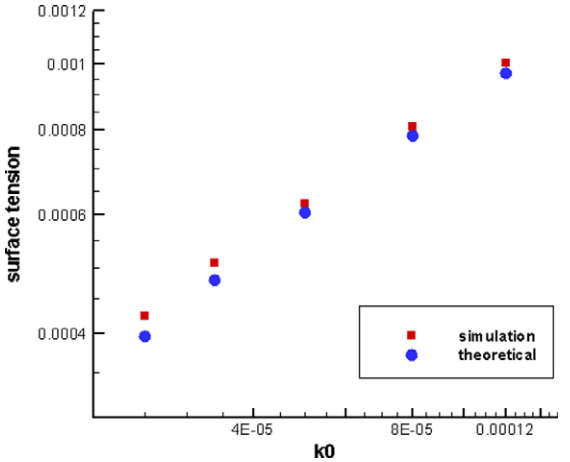

Fig. 5. Relation between surface tension and parameter k_0. Theoretical values are obtained from Eq. (13).

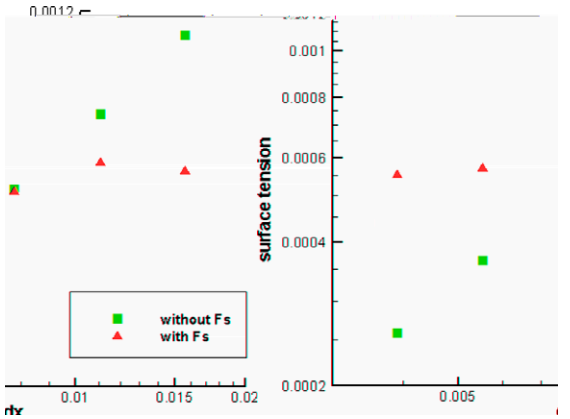

Fig. 6. Change of surface tension as a function of the grid size. Two series of simulations are performed using interaction force in Eq. (8) (without $\mathbf{F}_s$), and in Eqs. (14) and (15) (with $\mathbf{F}_s$), respectively.

(20). In the improved model, Eqs. (14) and (17) are used instead of Eq. (8) to introduce adjustments of the interaction force, and Eqs. (21)–(23) replace Eqs. (1), (3), (19) and (20) to implement Guo's forcing scheme.

Table 1 shows an example of the different equilibrium properties obtained by using Guo's forcing scheme and the original Shan–Chen forcing scheme. The interaction potential is chosen to be

$$\psi(\rho) = \exp(-1/\rho) \tag{24}$$

The simulation was performed in a periodic domain with flat interfaces between the two phases. With a fixed interaction strength $G = -10$, the simulation was conducted for different the grid size Δx, which leads to a varying τ according to Eq. (5). Ideally, the equilibrium properties of the fluid should be independent of the grid size, which is the case in the results obtained from Guo's forcing scheme. However, with the original forcing scheme in Shan–Chen model, the equilibrium densities and pressure are found to be changing with grid size and consequently with τ. Through extensive investigation, it is found that this unfavorable feature of Shan–Chen forcing scheme exists for all equations of state, and the resulted density ratio ρ_l/ρ_v decreases with the increase of τ. The calculated equilibrium densities and pressure only approaches the theoretical value with a vanishing viscosity, which is equivalent to $\tau = 0.5$. The deviation is mainly in the gas phase density, which changes about 20% in this case when τ changes from 0.548 to 1.268. The deviation could be much more severe in the case of a low quench temperature (T/T_c), or a high density ratio. For example, if Carnahan–Starling equation of state is used at $T/T_c = 0.76$, the equilibrium gas density will change from 0.0122 to 0.00043 when τ changes from 1 to 0.506. As the result, the equilibrium pressure will drop from 7.7×10^{-4} to 3.1×10^{-5}, and the density ratio will increase dramatically from 26.8 to 747.8. The independence of equilibrium properties from τ in Guo's forcing scheme makes it a superior choice to the Shan–Chen forcing scheme, and the difference of the two schemes can be shown to be on the order of $O(\mathbf{F}^2)$. The dependence of equilibrium properties on τ in Shan–Chen model has not been discussed extensively in the literature, since in most two-phase simulations both viscosity and mesh size are fixed, and therefore τ is a constant. However, if grid size is allowed to change, it is inevitable to yield different values of τ in the same computational domain. Therefore, in order to achieve consistent equilibrium properties in the entire domain, Guo's forcing scheme is used for all the results presented in the following sections.

Table 2 compares the numerical and theoretical equilibrium properties at various values of G. The density ratio between the two phases increases with an increasing magnitude of G, and the difference between the numerical and theoretical values are very small in all cases. A good agreement between theoretical and numerical results can also be found in Fig. 4, which shows the density profiles for three cases with different values of G. Table 2 and Fig. 4 indicate that the equilibrium properties as well as the density profile can be accurately predicted using Eq. (12).

The relation between k_0 and surface tension is presented in Fig. 5. Theoretical values of the surface tension are calculated from Eq. (13). The numerical results of the surface tension are in good agreement with the theoretical prediction. It is noted

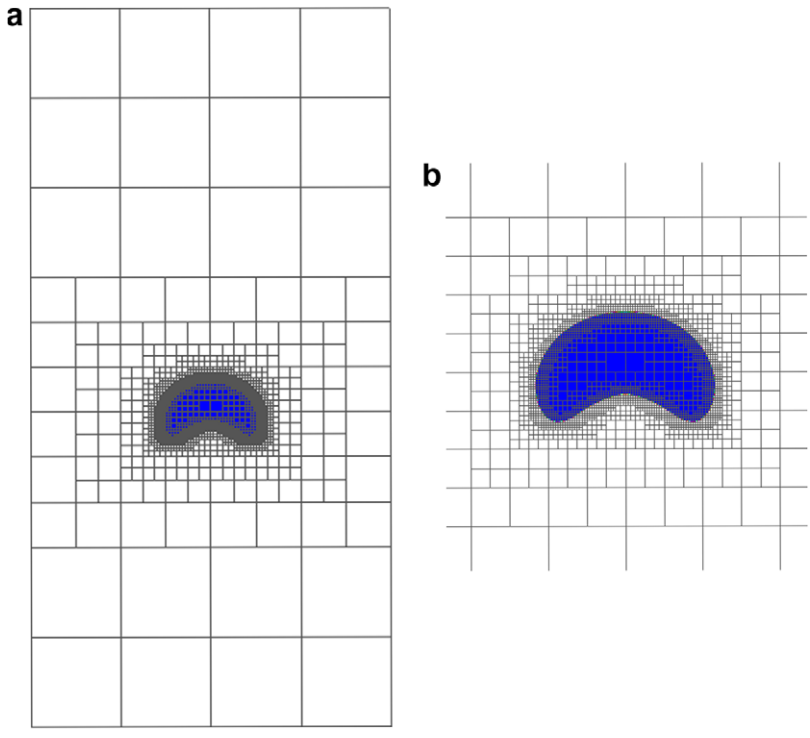

Fig. 7. Grid arrangement for case S3. (a) Entire computation domain and (b) close-up of bubble region.

that the form of the interface stress in Eq. (14) is also employed in other diffuse interface methods to specify the gradient energy at the interface [5]. From the analysis in those studies, the surface tension is roughly proportional to the square root of k_0. This trend is also observed in this study by investigating the slopes in Fig. 5. The LBM simulation gives $\sigma \propto k_0^{0.55}$, while the prediction by Eq. (13) gives a slightly different relationship, which is $\sigma \propto k_0^{0.57}$. This indicates that the parameter k_0 provides a predictable way to adjust the surface tension.

Table 3
Summary of simulation conditions for bubble flows. Cases S, M, and D stand for 2D single-component, 2D multi-component, and 3D multi-component LBM models.

Case	*Eo*	*Mo*	*Re*	Shape
S1	15.28	13.57	1.26	Oblate ellipsoidal cap
S2	43.40	27.15	2.52	Oblate ellipsoidal cap
S3	49.82	137.42	1.91	Oblate ellipsoidal cap
S4	62.28	135.73	2.14	Oblate ellipsoidal cap
S5	99.65	274.85	2.70	Oblate ellipsoidal cap
S6	86.80	54.29	3.08	Oblate ellipsoidal cap
S7	2.06	1.7E−05	18.34	Oblate ellipsoidal
S8	10.31	8.48E−05	23.16	Oblate ellipsoidal
M1	23.06	0.33	6.14	Spherical cap
M2	38.44	0.55	8.18	Spherical cap
M3	0.08	2.31E−05	0.56	Spherical
M4	0.27	2.31E−05	2.27	Spherical
M5	0. 67	2.31E−05	6.39	Spherical
M6	1.33	2.31E−05	10.64	Spherical
M7	4.32	2.31E−05	28.30	Oblate ellipsoidal
M8	7.68	2.31E−05	39.36	Oblate ellipsoidal
D1	2.45	2.98E−05	18.20	Oblate ellipsoidal
D2	9.81	1.19E−4	36.24	Oblate ellipsoidal
D3	31.36	0.21	10.97	Oblate ellipsoidal cap

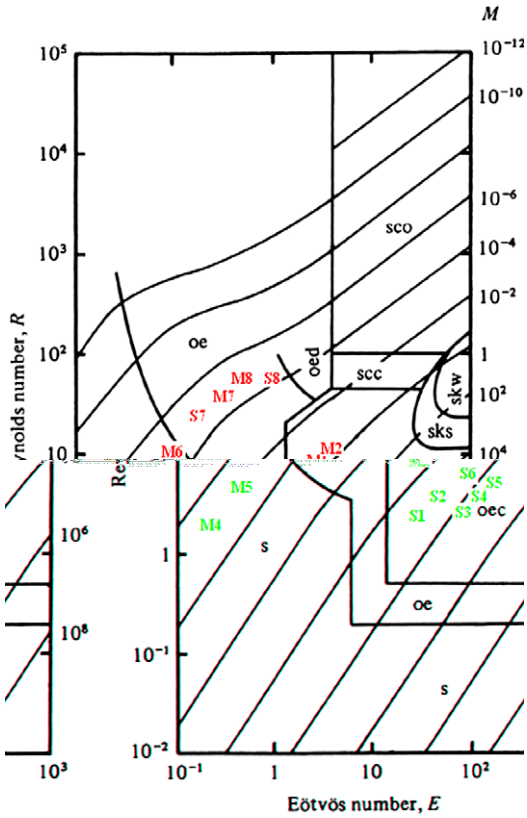

Fig. 8. Corresponding locations of current simulation cases in the regime diagram given by Bhaga and Weber [39].

When non-uniform grid size is used, the surface tension in the original interaction force specified in Eq. (8) may change with the grid size, as shown in Fig. 6. The slope in the log–log plot in Fig. 6 is found to be 1.03, which indicates the relation $\sigma \propto \Delta x$ in the original interaction force model. In fact, the same linear relationship can be found analytically by combining Eqs. (12) and (13). By introducing the correction term $\mathbf{F}_s$ in Eq. (14), the surface tension value can be tuned to stay constant as grid size changes.

The analysis and simulations above emphasize the relationship between grid sizes and fluid properties such as phase equilibrium and surface tension in the interaction potential model. In the original Shan–Chen model, fluid properties cannot remain constant on different mesh size. However, consistent fluid properties can be achieved by applying Guo's forcing scheme [37] and by introducing correction terms in the interaction force. It is also demonstrated that the theoretical analysis by Shan [35] gives accurate prediction of the properties in the interaction potential model, and thus, can be used as a guide to adjust simulation parameters and to assign initial conditions for the simulation.

4.4. Integration of multiphase LBM with AMR

The computation procedure of multiphase LBM on a non-uniform mesh is essentially the same as the single phase algorithm described in Section 3, and the only additional step is incorporation of the interaction force. Calculation of the force involves taking the gradient of the potential, which requires information from neighboring cells. When this occurs at the coarse–fine grid interface, the potential on the other side of the interface can be easily averaged/interpolated and then communicated across the block boundary. Once the force is obtained, the forcing scheme itself is a local operation and can be performed at the same time as the collision step.

The adaptive refinement of the mesh takes place every few steps in the simulation. For multiphase flows which involve two-fluid phases with different densities, it is natural to use the magnitude of density gradient as the criterion for mesh refinement. The interface between two phases is located by finding the blocks whose density gradient is above a critical value, and these blocks are assigned to be at the highest refinement level. Regions away from the interface have successively larger grid size. It is important that the highest and lowest refinement levels are specified to avoid infinite refinement or excessive coarsening during the simulation.

5. Simulation of bubble flows

A bubble rising in a viscous liquid medium is a typical two-phase flow problem that has been studied extensively using both experimental and numerical approaches. In such flows, both the rise velocity and the bubble shape are determined by the properties of the gas and liquid phases as well as the magnitude of the gravitational force. These complicated non-linear relations are often correlated in terms of three dimensionless groups, including the Reynolds number (*Re*), the Eötvös number (*Eo*), and the Morton number (*Mo*):

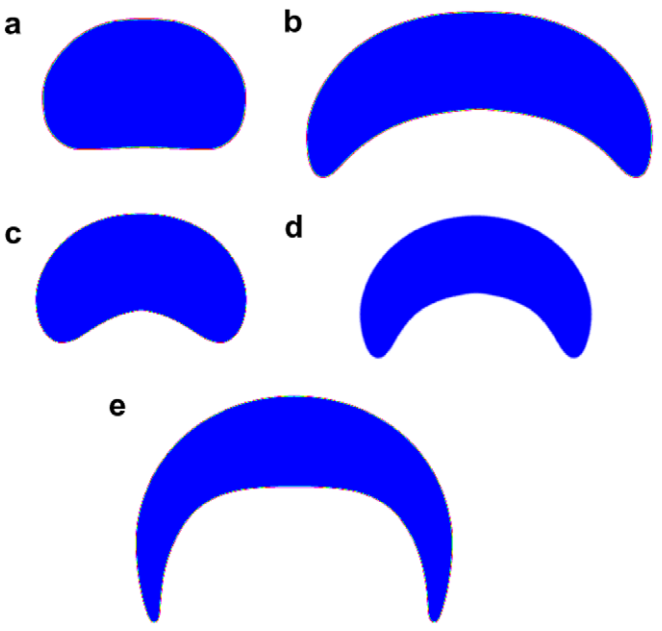

Fig. 9. Simulated shapes of oblate ellipsoidal cap bubbles. (a) Case S1: *Eo* = 15.3, *Mo* = 13.6. (b) Case S2: *Eo* = 43.4, *Mo* = 27.1. (c) Case S3: *Eo* = 49.8, *Mo* = 137.4. (d) Case S4: *Eo* = 62.3, *Mo* = 135.7. (e) Case S5: *Eo* = 99.6, *Mo* = 274.9.

$$Re = \frac{\rho d U}{\mu} \tag{25}$$

$$Eo = \frac{\rho g d^2}{\sigma} \tag{26}$$

$$Mo = \frac{g\mu^4}{\rho\sigma^3} \tag{27}$$

In the above equations, ρ and μ are the density and viscosity of the liquid, d is the equivalent diameter of the bubble, U is the rising speed of the bubble, g is the acceleration of gravity, and σ is the surface tension coefficient of the gas–liquid interface. The bubble regime diagrams made by Grace [38], and later modified by Bhaga and Weber [39], are well-known graphical representations of such correlations.

In recent years, various direct numerical simulation techniques have been applied to study the bubble rise behavior. Van Sint Annaland et al. [40,41] simulated different bubble regimes using the both VOF and front-tracking methods. By VOF method, they simulated condition where *Eo* ranged from O(1) to O(10^2), and *Re* from O(1) to O(10). Using front-tracking method, they could simulate much a wider range of the parameters, with *Eo* ranged from O(1) to O(10^2), and *Re* from O(1) to O(10^3), covering the spherical regime, ellipsoidal regime, and intermediate *Re* portion of the spherical cap regime. Yu and Fan [42] performed similar simulations with the level-set method, and focused on the conditions with high *Re* ($\sim 10^3$) and large deformation ($Eo \sim 10^2$). Simulations concerning the interactions between multiple bubbles in a cluster have been conducted by Bunner and Tryggvason [43]. There are several studies that apply LBM to investigate bubble dynamics, but only a few have reported convincing results by validating the simulation with experiment data, especially under different conditions. Sankaranarayanan et al. [30] used implicit formulation of the interaction potential based LBM to study the

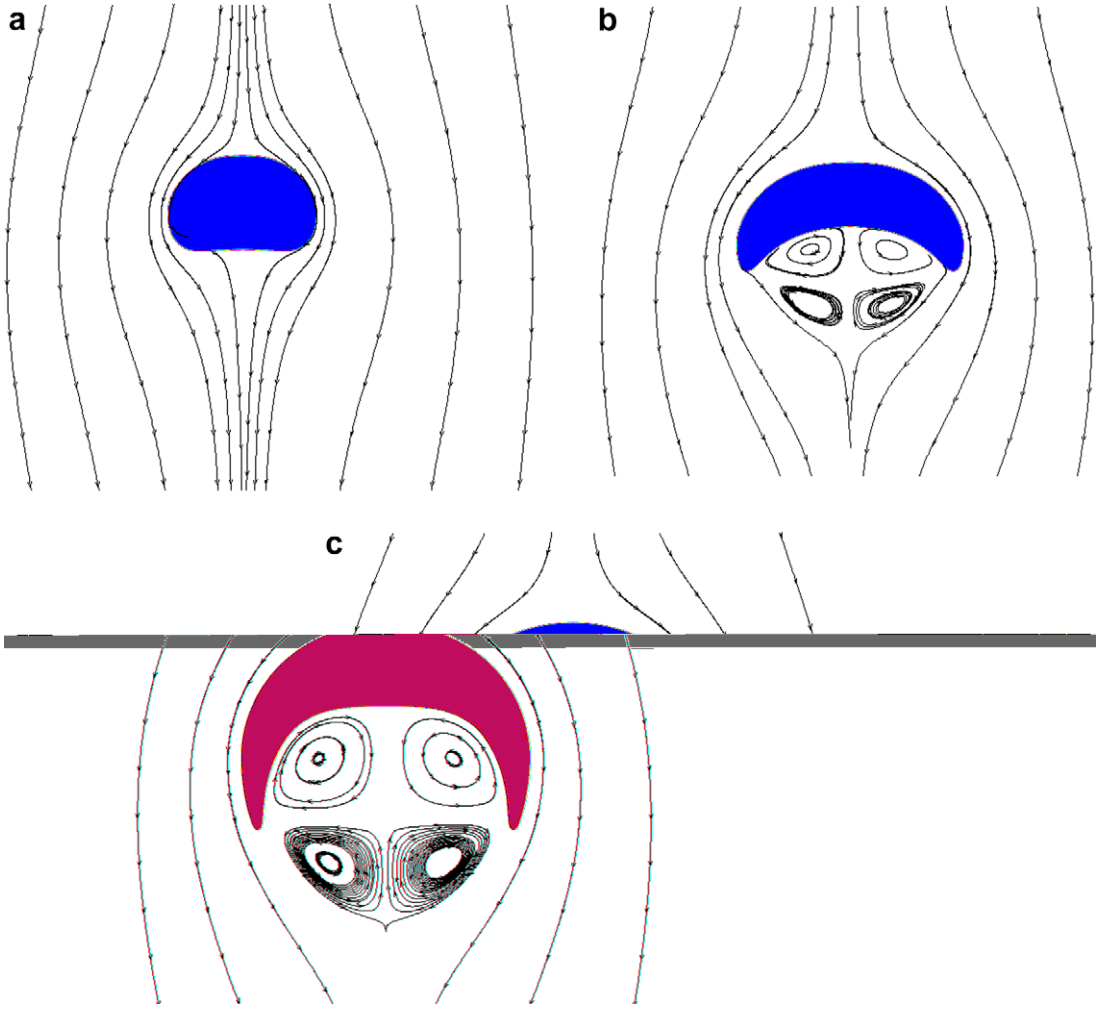

Fig. 10. Streamlines of relative velocity. (a) Case S1; (b) case S2; and (c) case S5.

drag and virtual mass forces on bubbles. They obtained closures relations of those forces for regular array of spherical and slightly distorted bubbles with *Eo* between $O(10^{-2})$ and $O(10^{2})$, and *Re* about 100–400. Other versions of LBM have also been employed to study the dynamics of bubbles, mainly in the spherical and ellipsoidal regimes [44,45]. In the simulations performed in the current study, the new LBM–AMR approach is employ to investigate the buoyant rise of bubbles under various conditions.

A typical grid set-up used in this study is shown in Fig. 7, with a close-up view of the grid refinement near the bubble. For single component multiphase simulation, usually 5–7 refinement levels are employed. Periodic conditions are applied for all boundaries of the computation domain. The bubbles are assumed to initially have spherical shapes, and the estimated fluid densities in the gas and liquid phase are assigned to the regions in and out of the initial bubble. The simulations then run without the presence of gravity for a certain period of time until the two phases reach equilibrium and the bubble volume remains constant. This initialization process usually takes a few thousand steps, depending on the accuracy of the initial guess of the densities. After initialization, gravity is turned on using the standard technique for bubble simulations [43,30], which is able to maintain the total momentum conservation of the entire simulation domain.

Table 3 lists the simulation conditions for all the cases discussed in this study. Their corresponding locations on the regime diagram [39] are marked in Fig. 8. The simulations S1–S8 are performed using 2D single component model, in which the interaction potential of the fluid is calculated using Eq. (24), with the interaction strength $G = -10.0$. The simulations M1–M8 and D1–D3 are performed with interaction model for binary components in 2D and 3D, respectively. In the two-component model, the first component is assumed to have a non-ideal EOS determined by Eq. (24), while the second component is assumed to be ideal gas. Although the multi-component model is more demanding in terms of computation time and memory usage, it appears to be more stable, especially for 3D cases. With $Eo < 0.1$, the current case M3 is outside the boundary of the diagram and therefore is not shown in Fig. 8.

Fig. 9 presents the simulated shapes of oblate ellipsoidal cap bubbles. These bubbles are characterized by increased aspect ratio as well as the indentation at the bottom. Fig. 9 suggests that the dimensionless width of the deformed bubble (the actual bubble width divided by its equivalent diameter) increases monotonically with *Re*, which is in agreement with the experimental observation reported by Bhaga and Weber [39]. Generally, the dented region also grows with the Reynolds number and the Eotvos number. Fig. 10 shows typical flow patterns by plotting the streamlines drawn with the relative velocity, which is the absolute velocity subtract the bubble velocity. When the bubble deformation is small and no significant dent is present at the bubble base, the liquid passes the bubble smoothly without the formation of vortices. As the deformation becomes more significant with larger dented area, two pairs of counter-rotating vortices start to form in the dented area. For such large bubbles, information of the flow inside the dented region is difficult to obtain experimentally and earlier researchers speculated that a pair of secondary vortices with reverse motion would be necessary in the internal circulation of the bubble to satisfy the velocity and stress continuity [2]. However, instead of being inside the bubble, the secondary vortex appears to be in the dented region outside the bubble as demonstrated by most recent numerical studies using front-tracking [18], level-set [42], and LBM [44]. The results obtained in this work are consistent with those in above numerical studies.

With further increase in Reynolds number, the indentation becomes more significant and the rear of the bubble gets more stretched. In this process, the thickness of bubble tail keeps decreasing, and the bubble shape becomes closer to the skirted regime. AMR techniques can provide the sufficient grid resolution that is required to resolve the thin skirt region, as shown

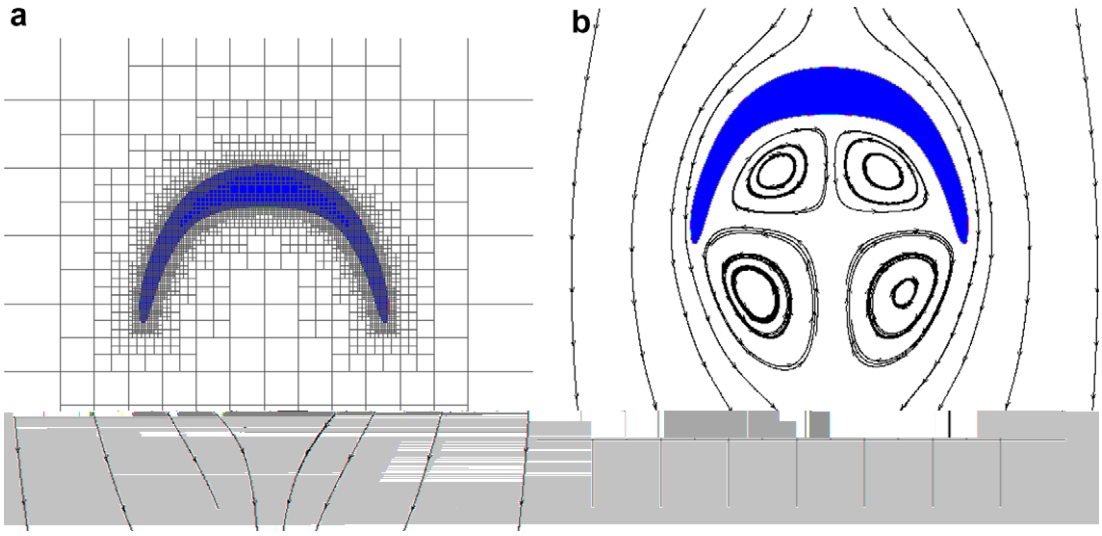

Fig. 11. Skirted bubble. *Eo* = 86.8, *Mo* = 54.3. (a) Grid configuration and (b) relative streamlines.

in Fig. 11(a). The streamlines are shown in Fig. 11(b), which have the similar vortex pattern as case S5 in the ellipsoidal cap regime, but with large size and further stretched in the flow direction.

For smaller bubbles in a less viscous liquid, both the Eotvos number and Morton number become reduced. There is smaller deformation of the bubble shapes, and they often appear in spherical or ellipsoidal shapes. Two cases with ellipsoidal bubbles are presented in Fig. 12. For case S7 with a smaller *Eo* and *Re*, the bubble rises in a rectilinear manner, and keeps the steady ellipsoidal shape. In case S8 with a slightly higher *Eo* and *Re*, the bubble follows a straight path initially when it gradually develops into the ellipsoidal disk shape, but then both the bubble shape and the path starts to oscillate. The oscillation pattern during bubble rise is often observed in a liquid with small viscosity such as water, which results in a small Morton number. The simulated condition ($Mo = 8.5 \times 10^{-5}$, $Eo = 10.3$) corresponds to a more viscous liquid. Tomiyama et al. [46] studied air bubbles in glycerol–water solutions, and found the oscillatory behavior for a bubble with a diameter of 5.5 mm, which corresponds to $Mo = 3.0 \times 10^{-6}$, and $Eo = 5.8$. In the numerical simulation by Theodoropoulos et al. [47], bubbles were found to oscillate when $Mo = 4.1 \times 10^{-4}$, and $Eo = 5.33$. The conditions in current case S8 fall between the two cases in above two studies. Two snapshots of the streamlines in cases S7 and S8 are compared in Fig. 12(c) and (d). The streamlines for the rectilinearly rising bubble is symmetric about its vertical axis, which is parallel to the flow direction. On the contrary, the orientation of the oscillating bubble varies with time and the flow past the bubble is highly asymmetric, with vortex formation behind the bubble.

Spherical cap shaped bubbles are simulated in cases M1 and M2, as depicted in Fig. 13. Compared to ellipsoidal cap bubbles, the spherical cap bubbles have a higher Reynolds number, and a more flat base with little indentation and therefore only one pair of large vortices are seen in the wake region.

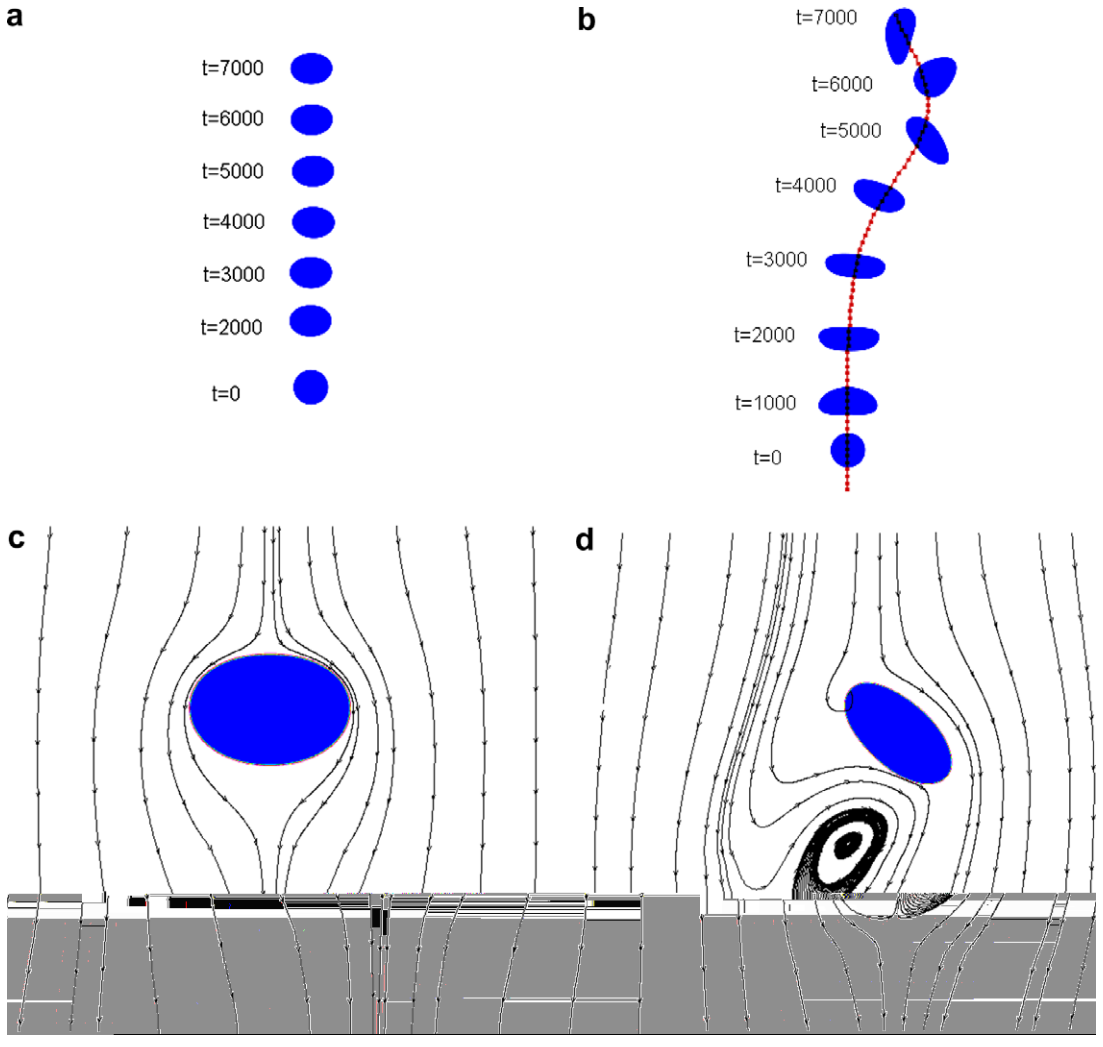

Fig. 12. Comparison of paths and streamlines for ellipsoidal bubbles. (a) Rectilinear path in case S7, *Eo* = 2.1, $Mo = 1.7^{-5}$, *Re* = 18.3. (b) Oscillatory path in case S8, *Eo* = 10.3, $Mo = 8.5^{-5}$, *Re* = 23.2. (c) Streamline in case S7. (d) Streamline in case S8.

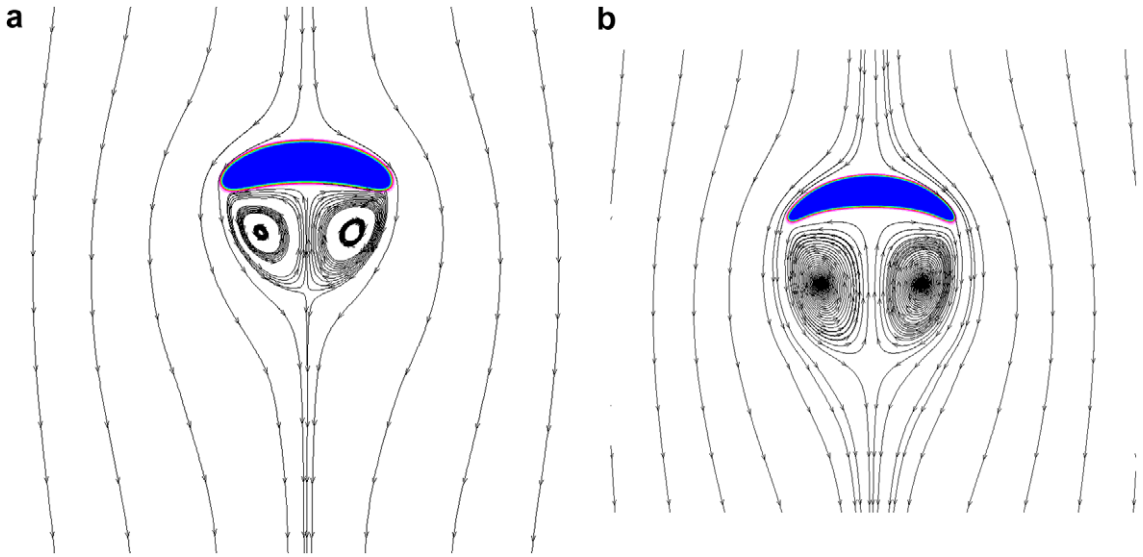

Fig. 13. Spherical cap bubble in case M (a) case M1, *Eo* = 23.06, *Mo* = 0.33 (b) case M2, *Eo* = 38.44, *Mo* = 0.55.

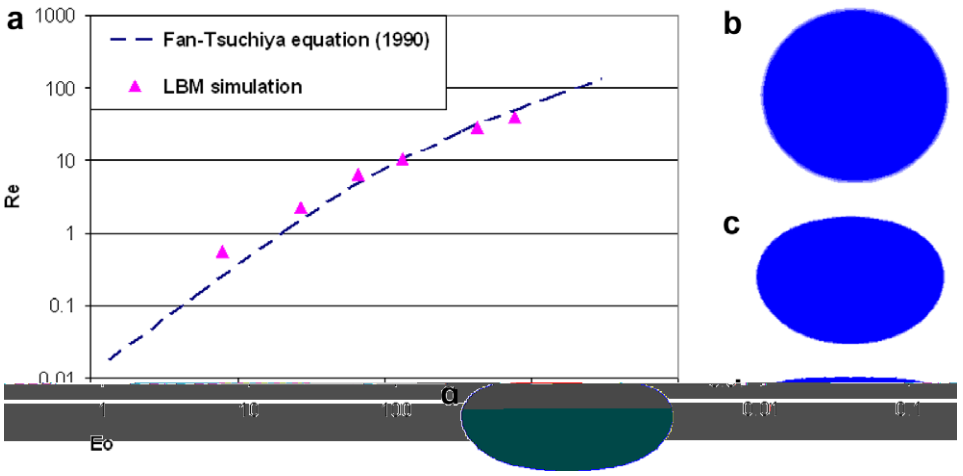

Fig. 14. Rise velocity of ellipsoidal bubbles (a) Comparison of simulated bubble rise velocity with Fan–Tsuchiya correlation [3] in Eq. (23). The bubbles have a fixed *Mo* of 2.3×10^{-5}, and *Eo* varies from 0.08 to 7.68 by changing the bubble size. (b) Bubble shape in case M5, *Eo* = 0.67. (c) Bubble shape in case M6, *Eo* = 1.33. (d) Bubble shape in case M8, *Eo* = 7.68.

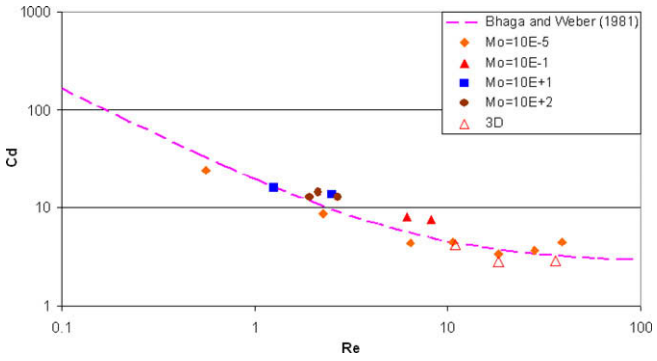

Fig. 15. Variations of the drag coefficient with the Reynolds number. The dashed line represents the experimental correlation by Bhaga and Weber [39], which is given in Eq. (26).

In cases M3–M8, a series of bubbles with same Morton number ($Mo = 2.3 \times 10^{-5}$) are simulated, which correspond to varying only the bubble size while keeping all fluid properties constant as in real experiments. With the Eotvos number varying from 10^{-1} to 10, the bubble gradually transform from spherical to ellipsoidal shape, as shown in Fig. 14(b)–(d). Many correlations exist for predicting the rise velocity of the bubble. Here the terminal velocities obtained from the simulation are compared against Fan and Tsuchiya's [3] correlation, which combines the linear prediction for low Reynolds number with the Mendelson equation for intermediate Reynolds numbers:

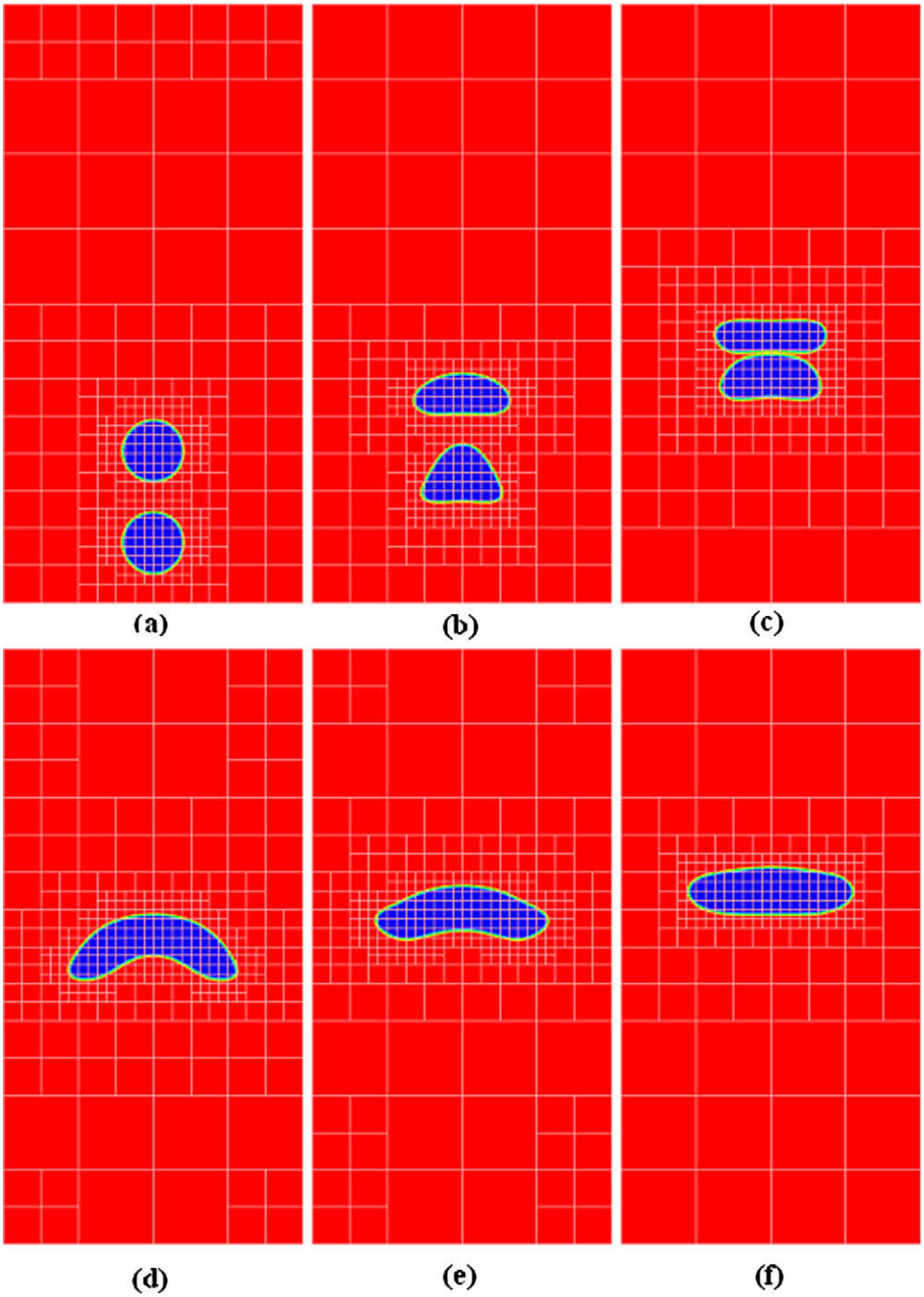

Fig. 16. Coalescence of two bubbles. $Mo = 1.5 \times 10^{-4}$, $Eo = 8.3$. The adaptive refinement of the mesh is shown in the background. Each square represents a block with 8×8 uniform meshes.

$$u_b = \left(\frac{\sigma g}{\rho}\right)^{1/4}\left[\left(\frac{Eo}{K_b Mo^{1/4}}\right)^{-n} + \left(\frac{2C}{Eo^{1/2}} + \frac{Eo^{1/2}}{2}\right)^{-n/2}\right]^{-1/n} \tag{28}$$

In the equation, K_b, C, and n are parameters determined by the liquid property and surface condition, and are chosen to be 15, 1.2, and 1.0, respectively. Both the predictions from Eq. (23) and the numerical results of the velocities are shown in Fig. 14, and a good agreement is found between the two.

In Bhaga and Weber's [39] experiments, the relation between drag coefficient and the Reynolds number were shown to be presented by a single curve for small Reynolds numbers ($Re < 10$) regardless of the Morton number. This curve is given by

$$C_D = [(2.67)^{0.9} + (16/Re)^{0.9}]^{1/0.9} \tag{29}$$

For the intermediate Reynolds number ($10 < Re < 100$), however, the $C_D - Re$ relationship may become a function of the Morton number. Fig. 15 shows the comparison between Eq. (24) and current simulations results, which have been grouped using Mo numbers. A reasonable agreement is achieved for the low Reynolds number part of the figure, and bubbles with different shapes have the same $C_D - Re$ relation. The deviation in C_D becomes larger as the Reynolds number approaches 10, which can be partly attributed to the dependence of C_D on the Morton number, and may also reflect the difference between the 2D simulations and the 3D experimental results.

The capability of LBM in modeling complex topology changes such as bubble breakage and coalescence is maintained in the LBM–AMR technique. Fig. 16 shows the coalescence of two equal sized bubbles with $Eo = 8.3$ and $Mo = 1.52 \times 10^{-4}$. The two bubbles are initially placed with a separation distance of 1.6D between their centers. Time sequences of the bubbles shape as well as the mesh refinement are provided in Fig. 16. The shape of the lower bubble is affected by hydrodynamic interaction between the two bubbles as it approaches the upper bubble. Squeezing of the thin liquid film between bubbles in their collision in seen at $t = 400$, and the rupture of the film leads to the coalescence shown in subsequent time frames.

The 3D simulations are also performed for a few cases. A D3Q19 lattice is used with the multi-component interaction model, and the mesh refinement technique is essentially the same as that in the 2D simulation. Fig. 17 shows the simulation results for the oblate ellipsoidal bubbles in cases D1 and D2. In case D1, with the Eo number of 2.45, the bubble is only slightly deformed. No vortices are found behind the bubble in the relative velocity field in Fig. 17(a). In case D2, the bubble shape has a higher aspect ratio as a result of the increased Eo number. A pair of symmetric vortices is seen in the streamlines behind the bubble. The Reynolds number in case D2 is 36, which is also higher than that in case D1. The evolution of the bubble in case D2 is shown in Fig. 18 with the mesh adaption process. Four levels of mesh are used in this case, and the adaption of the mesh resolution in accordance with the bubble motion is clearly demonstrated. Case D3 simulates the ellipsoidal cap bubble with $Eo = 31.36$ and $Mo = 0.21$. The dimple at the bubble base is clearly visible from the bottom view in Fig. 19(b).

In the simulations performed in this study, the gain in computation efficiency as a result of the adaptive mesh scheme relies on the number and size of bubbles as well as the number of refinement levels, and is therefore case-dependent. As

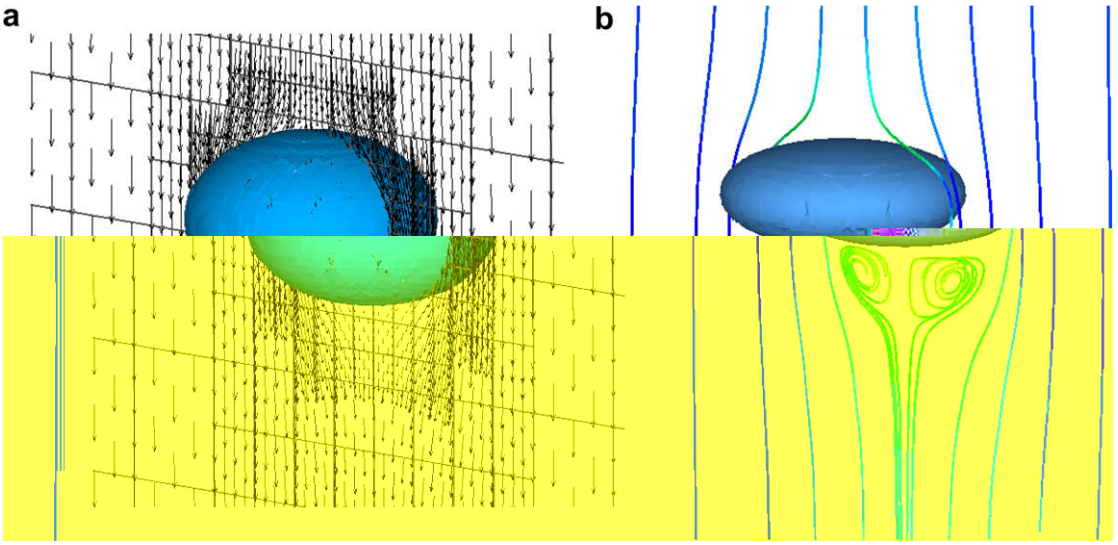

Fig. 17. 3D simulation of ellipsoidal bubbles. (a) Case D1. Eo = 2.45, Mo = 2.98E−05 (b) Case D2. Eo = 9.81, Mo = 1.19E−04.

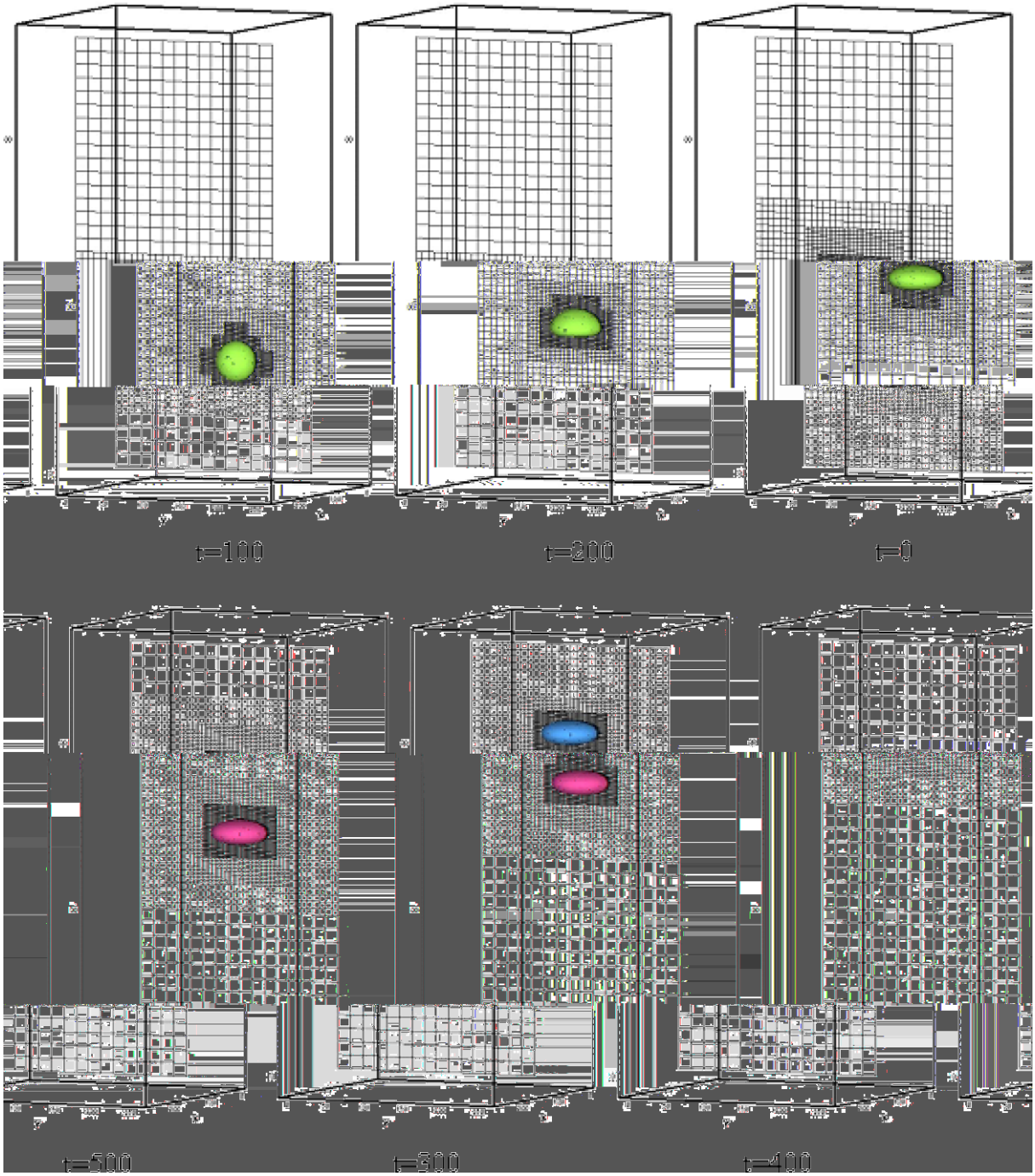

Fig. 18. Time sequence of 3D bubble rise in case D2.

a typical example, for a 2D single-component simulation of a bubble with diameter of 128 lattice units in a 1024×1024 domain, four levels of grid refinement can reduce the memory usage by about 78%, and reduce the computation time by about 95% compared to the uniform mesh with the finest resolution. Such comparison is based on the numerical experiments using the same computation code which utilizes the PARAMESH package for mesh management. It is noted that the PARAMESH package is not specifically built for LBM algorithms and it causes some redundancy in memory usage and sacrifice in efficiency. However, even compared to a separate program with straightforward implementation of LBM algorithm on a uniform mesh, the current LBM–AMR code (integrated with PARAMESH) with four levels can still reduce the computation time by about 50%.

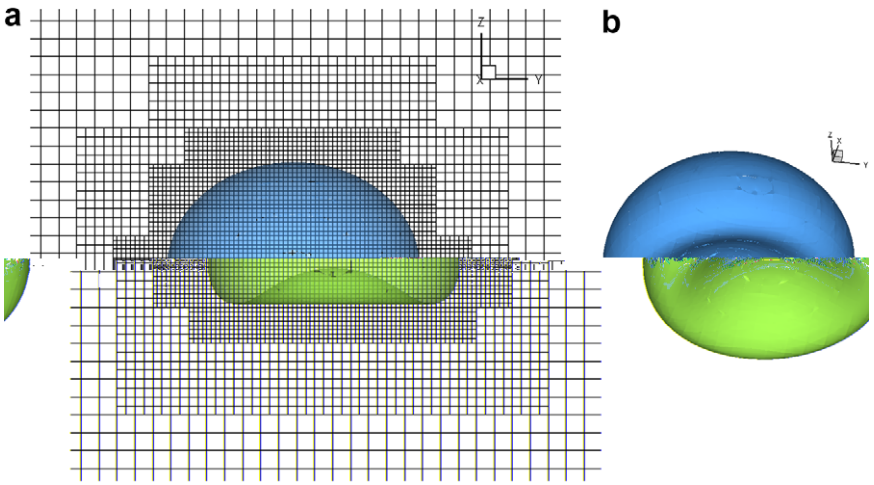

Fig. 19. 3D ellipsoidal cap bubble in case D3. *Eo* = 31.36, *Mo* = 0.21. (a) Grid configuration and (b) bottom view showing the dented region.

6. Concluding remarks

A lattice Boltzmann method with adaptive mesh refinement is developed for the simulation of two-phase flows. The traditional LBM algorithm based on uniform grids is extended to be able to operate on a non-uniform mesh by introducing special operations to communicate information between blocks with different grid sizes. The interaction potential model is adopted to generate two-fluid phases in equilibrium. Theoretical analysis and numerical tests have been performed to investigate the properties of the interaction potential model. It is demonstrated that the original Shan–Chen model cannot maintain consistent fluid properties when the grid size changes. To overcome this problem, the improved interaction potential model is introduced, which has the benefit of grid-independent equilibrium properties and adjustable surface tension. The newly developed LBM–AMR technique is validated through both single phase and two-phase flow simulations. The 2D and 3D bubble rising in viscous liquids are simulated under various conditions, and both bubble shape and rise velocity are found to be in good agreement with experimental data in the literature. The bubble shape and the flow field can be adequately resolved even under the condition of large bubble deformation. The original advantage of LBM in simulating large topology changes is maintained in the LBM–AMR algorithm, as demonstrated in the simulation of coalescence between two bubbles. This new LBM–AMR method greatly extends the capability of LBM in multiphase flow simulation by improving the accuracy at the interface between two phases, and reducing the computation cost for the entire computation domain. It is expected that together with other advanced techniques in LBM, the adaptive scheme developed in this work will enable the application of LBM in a broad range of complex multiphase flow problems that are relevant to real-world engineering practice.

Acknowledgments

Acknowledgement is made to the Donors of the American Chemical Society Petroleum Research Fund under Grant PRF #44515-AC9 for partial support of this research. The work is also supported in part by the Ohio Supercomputer Center.

References

[1] L.-S. Fan, Gas–Liquid–Solid Fluidization Engineering, Butterworth Publishers, Boston, 1989.
[2] R. Clift, J.R. Grace, M.E. Weber, Bubbles, Drops and Particles, Academic Press, New York, 1978.
[3] L.-S. Fan, K. Tsuchiya, Bubble Wake Dynamics in Liquids and Liquid–Solid Suspensions, Butterworth-Heinemann, Berlin, 1990.
[4] D.M. Anderson, G.B. McFadden, A.A. Wheeler, Diffuse-interface methods in fluid mechanics, Annual Review of Fluid Mechanics 30 (1998) 139–165.
[5] D. Jacqmin, Calculation of two-phase Navier–Stokes flows using phase-field modeling, Journal of Computational Physics 155 (1999) 96–127.
[6] S. Unverdi, G. Tryggvason, A front-tracking method for viscous incompressible multi-fluid flows, Journal of Computational Physics 100 (1992) 25–37.
[7] C.W. Hirt, B.D. Nichols, Volume of fluid (VOF) methods for the dynamics of free boundaries, Journal of Computational Physics 39 (1981) 201–225.
[8] M. Sussman, P. Smereka, S. Osher, A level set approach for computing solutions to incompressible two-phase flow, Journal of Computational Physics 114 (1994) 146–159.
[9] R.R. Nourgaliev, T.N. Dinh, T.G. Theofanous, D. Joseph, The lattice Boltzmann equation method: theoretical interpretation, numerics and implications, International Journal of Multiphase Flow 29 (2003) 117–169.
[10] X. Shan, X.-F. Yuan, H. Chen, Kinetic theory representation of hydrodynamics: a way beyond the Navier–Stokes equation, Journal of Fluid Mechanics 550 (2006) 413–441.
[11] S. Chen, G.D. Doolen, Lattice Boltzmann method for fluid flows, Annual Review of Fluid Mechanics 30 (1998) 329–364.
[12] X.W. Shan, H.D. Chen, Lattice Boltzmann model for simulating flows with multiple phase and components, Physical Review E 47 (1993) 1815–1819.
[13] M.R. Swift, E. Orlandini, W.R. Osborn, J.M. Yeomans, Lattice Boltzmann simulations of liquid–gas and binary fluid systems, Physical Review E 54 (1996) 5041–5052.

[14] A.K. Gunstensen, D. Rothman, Lattice Boltzmann model of immiscible fluids, Physical Review A 43 (1991) 4320–4327.
[15] I. Ginzburg, G. Wittum, Two-phase flows on interface refined grids modeled with VOF, staggered finite volumes and spline interpolants, Journal of Computational Physics 166 (2001) 302–335.
[16] M. Sussman, A.S. Almgren, J.B. Bell, P. Colella, L.H. Howell, L.M. Welcome, An adaptive level set approach for incompressible two-phase flows, Journal of Computational Physics 148 (1999) 81–124.
[17] E. Olsson, G. Kreiss, S. Zahedi, A conservative level set method for two phase flow II, Journal of Computational Physics 225 (2007) 785–807.
[18] J.S. Hua, J.F. Stene, P. Lin, Numerical simulation of 3D bubbles rising in viscous liquid using a front tracking method, Journal of Computational Physics 227 (2008) 3358–3382.
[19] O. Filippova, D. Hanel, Grid refinement for lattice-BGL models, Journal of Computational Physics 148 (1998) 219–228.
[20] A. Dupuis, B. Chopard, Theory and application of an alternative lattice Boltzmann grid refinement algorithm, Physical Review E 67 (2003) 066707.
[21] D. Yu, R. Mei, W. Shyy, A multi-block lattice Boltzmann method for viscous fluid flows, International Journal for Numerical Methods in Fluids 39 (2002) 99–120.
[22] Y. Peng, C. Shu, Y.T. Chew, X.D. Niu, X.Y. Lu, Application of multi-block approach in the immersed boundary-lattice Boltzmann method for viscous fluid flows, Journal of Computational Physics 218 (2006) 460–478.
[23] M. Rohde, D. Kandhai, J.J. Derksen, H.E.A. van der Akker, A generic mass-conservative local grid refinement technique for lattice Boltzmann scheme, International Journal for Numerical Methods in Fluids 51 (2006) 439–468.
[24] H. Chen, O. Filippova, J. Hoch, K. Molvig, R. Shock, C. Teixeira, R. Zhang, Grid refinement in lattice Boltzmann methods based on volumetric formulation, Physica A 362 (2006) 158–167.
[25] E. Fares, Unsteady flow simulation of the Ahmed reference body using a lattice Boltzmann approach, Computer and Fluids 35 (2006) 940–950.
[26] J. Tolke, S. Freudiger, M. Krafczyk, An adaptive scheme using hierarchical grids for lattice Boltzmann multiphase flow simulations, Computer and Fluids 35 (2006) 820–830.
[27] P. Yuan, L. Schaefer, Equation of state in a lattice Boltzmann model, Physics of Fluids 18 (2006) 042101.
[28] T. Inamuro, T. Ogata, S. Tajima, N. Konishi, A lattice Boltzmann method for incompressible two-phase flows with large density differences, Journal of Computational Physics 198 (2004) 628.
[29] T. Lee, C.-L. Lin, A stable discretization of the lattice Boltzmann equation for simulation of incompressible two-phase flows at high density ratio, Journal of Computational Physics 206 (2005) 16–47.
[30] K. Sankaranarayanan, X. Shan, I.G. Kevrekidis, S. Sundaresan, Analysis of drag and virtual mass forces in bubbly suspensions using an implicit formulation of the lattice Boltzmann method, Journal of Fluid Mechanics 452 (2002) 61–96.
[31] K.N. Premnath, J. Abraham, Three-dimensional multi-relaxation time (MRT) lattice Boltzmann models for multiphase flow, Journal of Computational Physics 224 (2008) 539–559.
[32] P. MacNeice, K.M. Olson, C. Mobarry, R. deFainchtein, C. Packer, PARAMESH: a parallel adaptive mesh refinement community toolkit, Computer Physics Communications 126 (2000) 330–354.
[33] X. He, G.D. Doolen, Thermodynamic foundations of kinetic theory and lattice Boltzmann models for multiphase flows, Journal of Statistical Physics 107 (2002) 309–328.
[34] J.S. Rowlinson, B. Widom, Molecular Theory of Capillarity, Oxford University Press, New York, 1982.
[35] X.W. Shan, Pressure tensor calculation in a class of non-ideal gas lattice Boltzmann models, Physical Review E 77 (2008) 066702.
[36] M. Sbragaglia, R. Benzi, L. Biferale, S. Succi, K. Sugiyama, F. Toschi, Generalized lattice Boltzmann method with multirange pseudopotential, Physical Review E 75 (2007) 026702.
[37] Z. Guo, C. Zheng, B. Shi, Discrete lattice effects on the forcing term in the lattice Boltzmann method, Physical Review E 65 (2002) 046308.
[38] J.R. Grace, Shapes and velocities of bubbles in rising in infinite liquids, Transactions of the Institution of Chemical Engineers 51 (1973) 116–120.
[39] D. Bhaga, M.E. Weber, Bubbles in viscous liquids: shapes, wakes, and velocities, Journal of Fluid Mechanics 105 (1981) 61–85.
[40] M. van Sint Annaland, N.G. Deen, J.A.M. Kuipers, Numerical simulation of gas bubbles behavior using a three-dimensional volume of fluid method, Chemical Engineering Science 60 (2005) 2999–3011.
[41] M. van Sint Annaland, W. Dijkhuizen, N.G. Deen, J.A.M. Kuipers, Numerical simulation of behavior of gas bubbles using a 3-D front-tracking method, AICHE Journal 99 (2006) 52.
[42] Z. Yu, L.-S. Fan, Direct simulation of the buoyant rise of bubbles in infinite liquid using level set method, Canadian Journal of Chemical Engineering 86 (2008) 267–275.
[43] B. Bunner, G. Tryggvason, Dynamics of homogeneous bubbly flows Part 1. Rise velocity and microstructure of the bubbles, Journal of Fluid Mechanics 466 (2002) 17–52.
[44] I.O. Kurtoglu, C.L. Lin, Lattice Boltzmann study of bubble dynamics, Numerical Heat Transfer B 50 (2006) 333–351.
[45] X. Frank, D. Funfschilling, N. Midoux, H.Z. Li, Bubbles in a viscous liquid: lattice Boltzmann simulation and experimental validation, Journal of Fluid Mechanics 546 (2006) 113–122.
[46] A. Tomiyama, H. Tamai, I. Zun, S. Hosokawa, Transverse migration of single bubbles in simple shear flows, Chemical Engineering Science 57 (2002) 1849–1858.
[47] C. Theodoropoulos, K. Sankaranarayanan, S. Sundaresan, I.G. Kevrekidis, Coarse bifurcation studies of bubble flow lattice Boltzmann simulations, Chemical Engineering Science 59 (2004) 2357–2362.